From helium to water: capillarity and metastability in two exceptional liquids

Frédéric Caupin

ÉCOLE NORMALE SUPÉRIEURE
DÉPARTEMENT DE PHYSIQUE

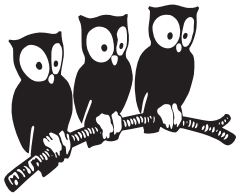

THÈSE D'HABILITATION À DIRIGER DES RECHERCHES
DE L'ÉCOLE NORMALE SUPÉRIEURE

présentée par

M. Frédéric CAUPIN

De l'hélium à l'eau : capillarité et métastabilité dans deux liquides d'exception

From helium to water: capillarity and metastability in two exceptional liquids

Soutenue le 2 Novembre 2009 devant le jury composé de :

M^{me} Christiane ALBA-SIMIONESCO	Examinatrice
M. Austen ANGELL	Rapporteur
M^{me} Élisabeth CHARLAIX	Présidente
M. Stéphan FAUVE	Examinateur
M. Laurent LIMAT	Examinateur
M. Detlef LOHSE	Rapporteur
M. Pierre-Étienne WOLF	Rapporteur

"The face of the water, in time, became a wonderful book [...].
And it was not a book to be read once and thrown aside,
for it had a new story to tell every day."

Mark Twain, *Life on the Mississippi*.

Acknowledgements

This manuscript reviews my research work since the end of my PhD thesis in 2000. I would like to thank all the members of the jury for their involvement in the evaluation of the present report.

Obviously, this research is not a task that I could have performed alone. I am indebted to all the members of the "Wetting and Nucleation" group of the Laboratoire de Physique Statistique, in particular Sébastien Balibar, Kristina Davitt, Claude Guthmann, and Etienne Rolley, and also to all the post-docs, students and visitors who have worked in the basement throughout these years; it is my pleasure to make a particular mention of my first PhD students, Eric Herbert and Arnaud Arvengas. My gratitude also goes to the researchers working in various institutions and countries who I had the luck and honor of collaborating with: Francesco Ancilotto, Ken H. Andersen, Cécile Appert, Manuel Barranco, Jordi Boronat, Hervé Cochard, Milton W. Cole, Humphrey J. Maris, Lionel Mercury, Tomoki Minoguchi, Alain Polian, Claire Ramboz, and Abraham D. Stroock.

A non negligible part of these years has also been devoted to teaching, which has given me the opportunity to try to communicate my interest in thermodynamics and experimental physics to the students. I want to express my thanks to all the people involved in the academic program of Physics at Ecole Normale Supérieure, at the "Formation Interuniversitaire de Physique" as well as at the "Préparation à l'Agrégation de Physique".

This work would not have been possible without the help of all the staff: the successive directors of the Laboratoire de Physique Statistique, Jacques Meunier and Eric Perez; the secretaries, Marie Gefflot, Annie Ribaudeau and Nora Sadaoui; the teams from the electronics and mechanic shops, and in particular Christophe Herrmann and José da Silva Quintas; the staff of the Department, and in particular Didier Courtiade, Zaïre Dissi, Jean-Claude Paindorge, and Allan Uguet. I thank them all and many other people who gave me help and advice; they are too numerous to be exhaustively listed here, and I hope they will forgive me for not mentioning their names.

Contents

1 Capillarity **13**
- 1.1 Grain boundaries in solid helium . . . 13
  - 1.1.1 Observations . . . 13
  - 1.1.2 Capillary model . . . 15
  - 1.1.3 Consequences . . . 17
- 1.2 Capillarity in nanopores . . . 19
  - 1.2.1 Capillary condensation . . . 19
  - 1.2.2 Capillary rise . . . 23
- 1.3 Density functional theory of interfaces . . . 24
  - 1.3.1 Density functional formalism . . . 24
  - 1.3.2 Liquid-vapor interface of water . . . 25
  - 1.3.3 Liquid-solid interface of helium . . . 26

2 Theoretical limits of metastability **29**
- 2.1 Theoretical background . . . 29
  - 2.1.1 Classical nucleation theory . . . 30
  - 2.1.2 Spinodal limits . . . 31
  - 2.1.3 Density functional theory of nucleation . . . 32
- 2.2 Stretched water . . . 32
  - 2.2.1 Competing scenarios . . . 32
  - 2.2.2 Density functional predictions for cavitation . . . 34
- 2.3 Metastable helium . . . 35
  - 2.3.1 Shape of the liquid-vapor spinodal . . . 35
  - 2.3.2 A liquid-solid spinodal? . . . 35
  - 2.3.3 Correction to classical nucleation theory . . . 36
- 2.4 Melting and freezing of nanoclusters . . . 37

3 Experimental study of metastable liquids **41**
- 3.1 Acoustic cavitation in water . . . 41
  - 3.1.1 Experimental setup . . . 42
  - 3.1.2 Statistics of cavitation . . . 43
  - 3.1.3 Estimate of the cavitation pressure . . . 43
  - 3.1.4 Comparison with other experiments . . . 44
- 3.2 Thermodynamic properties of metastable water . . . 46
  - 3.2.1 Density . . . 46
  - 3.2.2 Path dependent cavitation . . . 48
  - 3.2.3 Sound velocity . . . 49
- 3.3 Acoustic crystallization in helium . . . 49
  - 3.3.1 Heterogeneous crystallization . . . 50
  - 3.3.2 Homogeneous crystallization . . . 51

List of specific acronyms used in the text

Acronym	Meaning	Page of first occurrence
GB	grain boundary	13
CST	Cole and Saam theory	20
AFM	atomic force microscope	21
RH	relative humidity	21
DFT	density functional theory	24
EoS	equation of state	25
RY	Ramakrishnan-Yussouff method	26
DCF	direct correlation function	26
RLV	reciprocal lattice vector	28
SGA	square gradient approximation	28
CNT	classical nucleation theory	30
LLCP	liquid-liquid critical point	33
LDM	line of density maxima	35
NC	nanocrystal	37
FOPH	fiber optic probe hydrophone	46
PD	photodiode	46
MCP	metastable critical point	47

Introduction

Water and helium: two exceptional liquids

Water is the most familiar liquid, and yet it hides a number of secrets. An interesting website[1] lists a total of 66 anomalous properties of water. Probably the most famous one is its *density maximum*, which occurs near 4°C under atmospheric pressure: whereas usual liquids expand upon warming, water expands upon *cooling*, at least between 0 and 4°C.

This can be seen as a macroscopic manifestation of a fundamental microscopic property of water: the existence of *hydrogen bonds*. Each water molecule is made of one oxygen and two hydrogen atoms; the electronic charges are not uniformly distributed among the three atoms, which leads to an attraction of the hydrogen atoms towards the oxygen atoms of other molecules. The hydrogen bond is not a real permanent bond: it is weaker than the covalent bond inside the molecule, but still strong enough (around 5 times the thermal energy $k_{\mathrm{B}}T$) to determine a number of water properties. The distance between molecules is larger when a hydrogen bond is formed. At low temperature, many hydrogen bonds are present, and the liquid has a low density; when the temperature increases, hydrogen bonds are broken, and the density increases, which explains the unusual expansion of water upon cooling. In hexagonal ice, all the possible hydrogen bonds are formed, so that the density is even lower than the liquid, which explains why ice cubes float over water, and why the liquid-hexagonal ice equilibrium line has a negative slope in the phase diagram shown on Fig. 1.

Interestingly, helium 4 also has a line of density maxima, and even a line of density minima. But its most prominent peculiarity is a macroscopic manifestation of its quantum nature: superfluidity. Below a temperature of around 2 K, liquid helium becomes a *super*-fluid, able to flow without viscosity. This is one of its quantum properties. Another one is that, because of the quantum zero point motion of the light helium atoms, the solid phase forms only at high pressure: there is no triple point and the liquid can be observed down to the absolute zero (Fig. 1).

Capillarity and metastability

Capillarity covers all the phenomena associated with interfaces, like the shape of soap bubbles, or that of a liquid meniscus near a wall or in a pore.

Metastability describes the states of matter when it exists in a phase which is not the most stable one. An example of a metastable phase of water is the liquid phase, when cooled below 0°C under atmospheric pressure: if the water is pristine and its container very clean, the liquid will not freeze right away, and instead remain in a *supercooled* state. The droplets in a freezing drizzle are in this state, but they freeze

[1] http://www.lsbu.ac.uk/water/anmlies.html

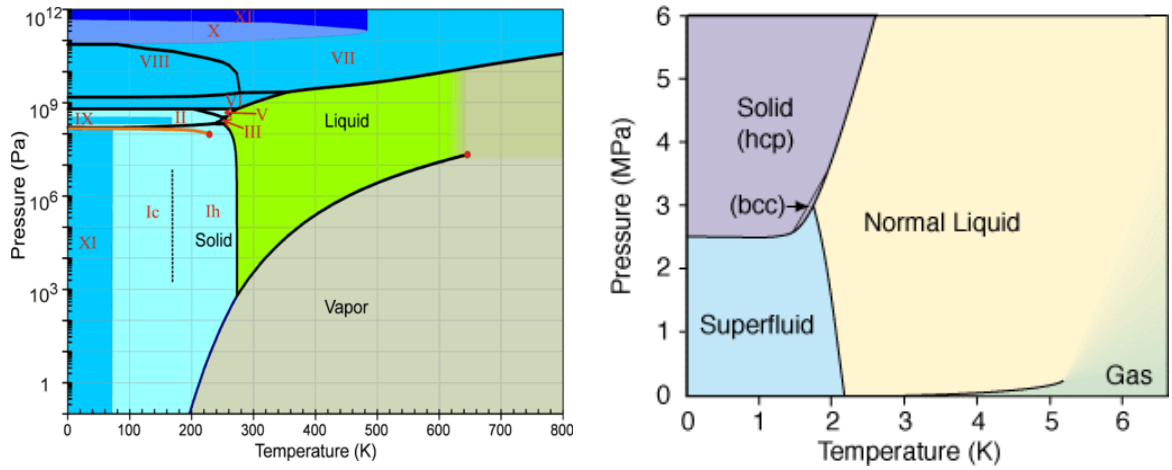

Figure 1: Phase diagram of water (left) and helium 4 (right) in the pressure-temperature plane.

when they hit the ground, which can have hazardous consequences. Similarly, a liquid can be *superheated* above its boiling point, until cavitation (the nucleation of bubbles) occurs.

Metastability is related to capillarity because of the importance of interfaces. Because of the relative stability of phases, it is energetically favorable to transform a metastable sample into the stable phase. However, for this to happen, the new phase has to nucleate, i. e. to appear as a tiny seed inside the metastable sample: this involves the creation of an interface which is energetically costly. The competition between the favorable volume energy and the costly interfacial energy results in an energy barrier to be overcome before the new phase can grow steadily.

In this report, we will illustrate the concepts of capillarity and metastability with examples mostly involving helium or water. The study of metastable liquids can bring original information about their structure. In the case of water, we have measured how far the liquid could be brought away from equilibrium with the vapor: we have thus explored the region of negative pressures, where the liquid is put under mechanical tension. Its density is then reduced, and the experiments probe the long range attraction part of the interaction between molecules. Our results point out a new anomaly of water in this region. In helium, we have explored another kind of metastability, this time by applying pressure above freezing: the liquid becomes denser and metastable compared to the solid. This raises interesting questions about the evolution of superfluidity, which is based on quantum exchange of atoms, when the atoms become more and more packed together.

Chapter 1 focuses on capillarity, with particular attention given to the liquid-solid interface of helium and the liquid-vapor interface of water. Some elements concerning adsorption in pores are also given. Chapter 2 discusses metastability from a theoretical point of view; it gives a quantitative relation with capillarity, and makes the connection between cavitation and the above mentioned lines of density maxima in helium and water. It also adresses the quantum properties of metastable helium, and makes a brief digression about nucleation in confined geometry. Chapter 3 summarizes our experiments on cavitation in water and crystallization in helium, based on the same acoustic technique.

Chapter 1

Capillarity

Capillarity is the study of interfacial phenomena. A recent book [1] gives an excellent introduction to the field. In this chapter we will review our contribution, which concerns mainly the liquid-solid interface of helium and the liquid-vapor interface of water. Section 1.1 reports an important experiment on grain boundaries in solid helium. We are interested in their wetting properties, i.e. how the interface between solid grains is wet by the liquid, and how it is affected by the cell walls. These properties have consequences in the debate about supersolidity of helium and also in the more general field of interfacial melting. An interpretation based on the simple capillary approximation, where interfaces are infinitely thin, will be described. Section 1.2 addresses the general topic of liquids confined in nanopores, where the interaction with the substrate must be taken into account. Section 1.3 goes beyond the capillary approximation, introducing density functional theory to treat interfaces.

1.1 Grain boundaries in solid helium

Helium can remain liquid down to the absolute zero (Fig. 1 in the Introduction). This makes it a unique substance which can be obtained with an outstanding purity. To produce solid helium, one has to apply pressures above 2.5 MPa, because of the quantum zero point motion of the very light helium atoms. Thanks to the high purity and low temperature, helium crystals can be grown with very few defects. The surface of helium crystals is a fascinating system which has been extensively studied, see Ref. [2] for a review. In particular, the liquid-solid interface is very mobile at low temperature, and is able to sustain the propagation of capillary waves, just as those generated by a small stone thrown in a pond. This makes helium one of the rare substances where the liquid-solid interfacial tension could be directly measured: σ_{LS} varies from 0.16 to 0.18 mJ m^{-2} depending on orientation [2]; in the following we will neglect this small anisotropy. We will now review our work on the interface between two crystals, which is called a *grain boundary* (GB).

1.1.1 Observations

In this section we describe our recent measurements of the wetting properties of GBs between helium crystals at low temperature (50 mK), made during the post-doc of Satoshi Sasaki [C1][1]. A detailed description of the experimental setup and procedure is given in Ref. [C2]. In brief, we use an optical dilution cryostat to look at crystals grown in a square cell whose dimensions are 11 mm × 11 mm × 3 mm. The small thickness of 3 mm is chosen so that the GBs lie in planes oriented nearly perpendicular to the two

[1] F. Caupin's publications cited in the text are distinguished from other references by the letter C, and two separate bibliographies are provided.

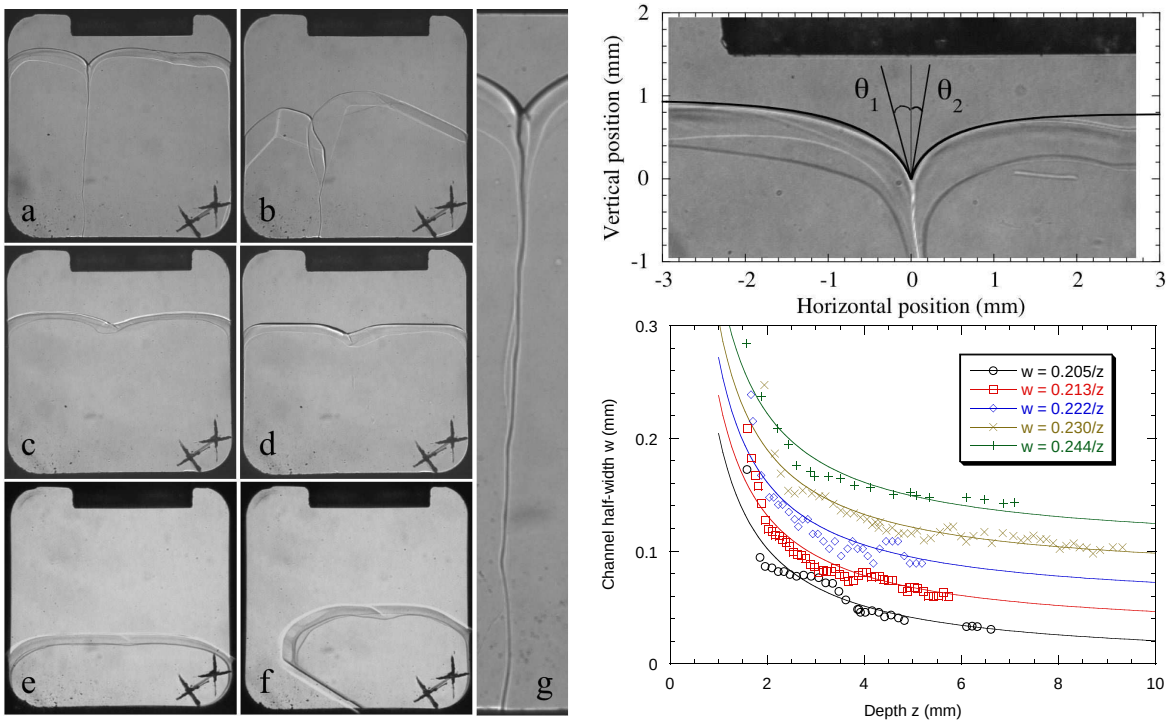

Figure 1.1: *Left panel*: Three couples of images showing equilibrium shapes (a,c,e) together with growth shapes which reveal the crystal orientation (b,d,f). When the two crystal grains have a large difference in orientation (a,b), their boundary ends as a deep groove at the liquid-solid interface. A zoom of (a) shows that the contact lines of the GB with the windows are in fact liquid channels (g). Crystals with similar orientations can be obtained by direct growth (c-f). In this case, the groove is shallow with no liquid channels on the windows. Two crosses carved on the windows (lower right corners) help adjusting the focusing. The cell dimensions are 11 mm × 11 mm × 3 mm. *Upper right panel*: The dihedral angle 2θ is determined by fitting each crystal profile with the Laplace equation near the groove nadir. *Lower right panel*: The half-width w as a function of depth z for 5 different samples. Good agreement with Eq. 1.4 is found. Each data set has been shifted upward starting from the lowest one, in increments of 0.025 mm to avoid overlaps [C1, C3].

windows, that is parallel to the optical axis. At the same time, 3 mm is large enough compared to the capillary length $l_c = \sqrt{\sigma_{LS}/\left[(\rho_S - \rho_L)g\right]} \simeq 1$ mm (g is the gravity and ρ_i the mass per unit volume of the phase i=L for liquid, S for solid), and to reduce the effect of the windows on the crystal shape at the center of the cell. Results in a thicker cell (10 mm) are qualitatively similar, but the GBs are not perpendicular to the windows, making quantitative measurements difficult. We shine parallel white light through the sample and take images with a CCD camera. Both liquid and solid are transparent, but they have a small difference in refractive index that makes the interface visible. To prepare a GB, we use the following procedure: we first fill the cell with liquid at a pressure near freezing; we then inject mass sufficiently rapidly to avoid closing the fill line with a solid plug, and we obtain a cell full of a solid sample with many grains;[2] we then melt the sample slowly until we keep only two grains which can finally be grown slowly to fill the lower part of the cell and exhibit a nearly vertical GB in the middle. An example of the bicrystal obtained is shown on Fig. 1.1 (a). When

[2]It is interesting to mention that we were able to detect strong light scattering from such samples, revealing the presence of inhomogeneities in density (for instance liquid droplets) with sizes comparable to the wavelength of light (600 nm) [C3].

the crystals grow at low temperature, they exhibit facets that reveal the difference in orientation (Fig. 1.1 (b)). Two main features appear in Fig. 1.1 (a): the groove at the liquid-solid interface and the two roughly vertical lines; see Fig. 1.1 (g) for a zoom.

The groove is created by the GB when emerging at the liquid-solid interface in order to satisfy the mechanical equilibrium between the three interfaces involved. We have measured θ_1 and θ_2, the angles at the nadir of the groove between the liquid-solid interface and the extrapolation of the GB plane into the liquid; the dihedral angle is then defined as $2\theta = \theta_1 + \theta_2$. The equilibrium condition is:

$$\sigma_{\rm GB} = \sigma_{\rm LS}(\cos\theta_1 + \cos\theta_2), \tag{1.1}$$

where $\sigma_{\rm GB}$ is the GB energy. Photographs such as the one displayed on Fig. 1.1 (upper right panel) show that θ is not zero, that is that the GB is not wet by the liquid, even at the liquid-solid equilibrium. In other words, the GB energy $\sigma_{\rm GB}$ is less than $2\sigma_{\rm LS}$. To measure θ_1 and θ_2, we fitted the interface profiles near the bottom of the groove with a one dimensional Laplace equation [C2]. We obtained $\theta = 11 \pm 3$, 16 ± 3, and $14.5 \pm 4^{\,o}$ for three different samples. The dihedral angle may vary from one sample to another, because of the various misorientation between the two grains.

We now turn to the roughly vertical lines on Figs. 1.1 (a,b,g). They correspond to liquid channels opening on the windows, because of the interfacial energy gained by replacing some solid on the window by the liquid. We have measured the channel width $2w$ and found that it was inversely proportional to the depth z below the top of the grains (Fig. 1.1, lower right panel). The liquid channel exists for all samples we made by fast injection. On the other hand, we could make two grains with similar orientation by nucleation in the cell in response to a pressure pulse made by closing a valve on the fill line (Figs. 1.1 (c-f)): they showed a shallower groove with larger θ (indicating a low energy GB, perhaps a stacking fault), and no liquid channel. These features can be explained with a simple capillary model described in the next section.

1.1.2 Capillary model

As shown on Fig. 1.1 (a,b,g), a liquid channel can exist at the contact line between the GB and the glass window of the cell. This phenomenon is due to the glass wall being preferentially wet, although not completely, by the liquid phase. It occurs when the GB energy $\sigma_{\rm GB}$ is large enough.

Figure 1.2 (a) shows a schematic view of a liquid channel. In the present treatment we neglect elasticity, and assume the surface tensions to be isotropic. Gravity and the force balance on the contact line between the liquid and GB then require the GB to lie in a vertical plane perpendicular to the wall, and the liquid channel to be symmetric with respect to this plane. Let $\theta_{\rm c}$ and $\theta_{\rm GB} = 2\theta$ be the contact angle of the liquid-solid interface on the wall, and the opening angle at the liquid-GB contact line, respectively. We have

$$\cos\theta_{\rm c} = \frac{\sigma_{\rm SW} - \sigma_{\rm LW}}{\sigma_{\rm LS}} \quad \text{and} \quad \cos\theta = \frac{\sigma_{\rm GB}}{2\sigma_{\rm LS}}\,, \tag{1.2}$$

where $\sigma_{\rm LS}$, $\sigma_{\rm SW}$, $\sigma_{\rm LW}$, and $\sigma_{\rm GB}$ the liquid-solid, solid-wall, liquid-wall, and GB surface tensions, respectively.

e and $2w$ are the maximum thickness and width of the liquid channel, and R the horizontal radius of curvature of the liquid-solid interface (see Fig. 1.2 (b)). Trigonometry gives the relations:

$$e = R\,(\cos\theta_{\rm c} - \sin\theta)\,, \tag{1.3}$$

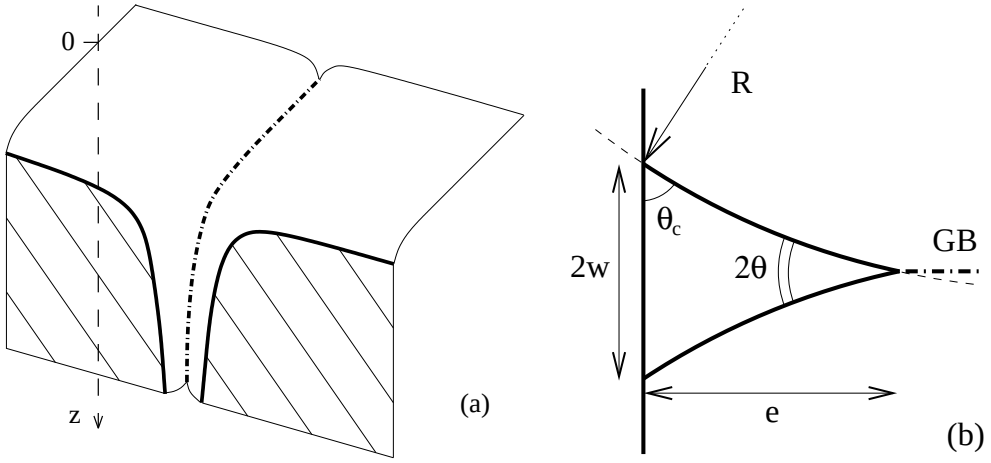

Figure 1.2: (a) Three dimensional view of the contact between a grain boundary (dash-dotted line) and a wall. The hatched area shows the contact of the wall with the solid. (b) Horizontal cross section of the liquid channel near the wall [C1, C3].

and

$$w = R\,(\cos\theta - \sin\theta_{\rm c})\,. \tag{1.4}$$

We can also calculate the cross section of the channel:

$$\Sigma = R^2\left[(\cos\theta_{\rm c} - \sin\theta)\,(\cos\theta - \sin\theta_{\rm c}) + \cos(\theta+\theta_{\rm c}) + \theta + \theta_{\rm c} - \frac{\pi}{2}\right]. \tag{1.5}$$

Our aim is to compute e and w as a function of the depth z. We take $z = 0$ at the flat liquid-solid interface at the top of the grains, where the pressure is the equilibrium pressure $P_{\rm eq}$ (see Fig. 1.2 (a)). Hydrostatic equilibrium in the liquid implies that the liquid pressure is $P_{\rm L}(z) = P_{\rm eq} + \rho_{\rm L} g z$. The chemical potential must be uniform:

$$\mu_{\rm L}[P_{\rm L}(z)] - gz = \mu_{\rm L}[P_{\rm eq}] = \mu_{\rm S}[P_{\rm S}(z)] - gz = \mu_{\rm S}[P_{\rm eq}] + \frac{P_{\rm S}(z) - P_{\rm eq}}{\rho_{\rm S}} - gz. \tag{1.6}$$

As $\mu_{\rm S}[P_{\rm eq}] = \mu_{\rm L}[P_{\rm eq}] = \mu_{\rm eq}$, this implies hydrostatic equilibrium in both phases: $P_{\rm L}(z) = P_{\rm eq} + \rho_{\rm L} g z$ and $P_{\rm S}(z) = P_{\rm eq} + \rho_{\rm C} g z$. The pressure difference through the liquid-solid interface sets its curvature. At depths large enough compared to the capillary length $l_{\rm c}$, the curvature in the horizontal plane dominates, and the liquid-solid interfaces in a horizontal plane are circular arcs of radius:

$$R = \frac{\sigma_{\rm LS}}{P_{\rm S}(z) - P_{\rm L}(z)} = \frac{{l_{\rm c}}^2}{z}\,, \tag{1.7}$$

with the liquid on the convex side. The measurements confirm that e and w are inversely proportional to z (Fig. 1.1, lower right panel); the coefficient is compatible with the value of the contact angle on the glass wall ($\theta_{\rm c} \simeq 45\,^{\rm o}$) that we have also measured directly [C2].

The liquid channel exists if and only if e and w are positive, that is $\theta_{\rm c} < \pi/2$, $\theta < \pi/2$, and $\theta + \theta_{\rm c} < \pi/2$. It is easy to see from Fig. 1.2 (b) that these are the conditions required to construct an arc with the correct contact angles, and the liquid on the convex side. This condition also explains why when θ is too large, as for the shallow grooves on Figs. 1.1 (c-f), the GB remains in contact with the window. Reasoning with the energy shows that, when the above conditions is satisfied, the channel is stable and that there is no energy barrier separating it from the state with no channel: it forms spontaneously [C2].

1.1.3 Consequences

Interfacial melting

At the free surface of a crystal, the particles are in a state intermediate between the bulk solid and the bulk liquid. Therefore it seems reasonable to expect that the free surfaces will melt more easily. This explains why, usually, a crystal cannot be superheated, that is heated to a temperature above its bulk melting temperature: it melts from its free surface. Surface melting has been observed experimentally; see for instance Ref. [3] for a review. What should we expect if the free surfaces are absent? This can be achieved by enclosing tightly the crystal in a box, or by heating only the center of a crystal away from its boundaries. One may expect that *internal* surfaces, namely the GBs in a polycrystal, may play a role: they could provide a favorable site for melting. The issue of GB melting has been a subject of debate [3]. Our observations on solid helium shed new light on the phenomenon.

We have found that the dihedral angle was always non zero, showing that the GB was only partially wet by the liquid, even at the liquid-solid equilibrium. It means that the thickness of the GB remains microscopic: it is not invaded by a thick liquid layer. This is in agreement with recent simulations [4], that found a GB thickness around 3 atomic layers. It is also consistent with a general argument from Lipowsky [5]: systems with long range forces, such as helium, should exhibit only partial GB wetting, whereas systems with short ranges forces can show complete wetting and premelting of a GB. In a review of this topic [C4], we have discussed other works on GB melting. A colloidal system, with short range forces, does show GB premelting [6]. Our findings also point out that observations on films, like those on the face centered cubic phase of helium at high pressure [7] must be taken with caution: liquid channels may exist at the contact between a GB and a wall; when the bulk melting temperature is approached, the channels could become as thick as the film and make the grains detach, even if bulk grains would not. The advantage of studying GB in helium is also to avoid melting due to impurities [3].

Supersolidity

Another consequence of our results lies in the context of *supersolidity* of helium. Superfluidity occurs when indistinguishable and delocalized particles can flow without resistance, as in liquid helium at low temperature. The supersolid state of matter would be realized when superfluidity coexists with the broken translational symmetry associated with the crystalline state. This topic was revived in 2004 with the experiments of Kim and Chan [8, 9]. They studied a torsional oscillator filled with solid helium 4. They noticed that the period of the oscillator dropped below a critical temperature around 200 mK, just as if part of the solid mass decoupled from the oscillating container. Furthermore, they observed that the period drop disappeared if the oscillator exceeded a critical velocity, and also if a barrier was put to block circular flow in a torsional oscillator with an annular channel. These features are similar to what is observed with *liquid* helium 4, with the difference that only part of the solid mass decouples, whereas all the liquid does. Moreover, the quantum nature of the atoms play a role: the effect, present with helium 4 which is a boson, was not detected with solid helium 3, made of fermions. These observations were interpreted as evidence for supersolidity, and triggered numerous theoretical and experimental investigations; see Ref. [C5] for a review.

Our contribution to the field deals with the search for continuous mass flow through

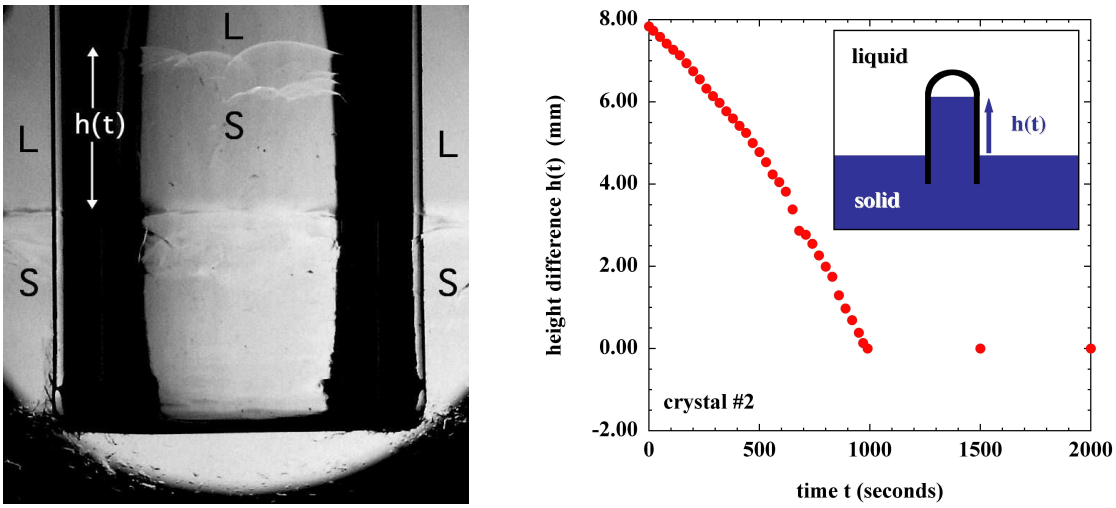

Figure 1.3: *Left*: Photograph of the Torricellian experiment on solid helium [C6, C7]. *Right*: Decrease of the inner liquid-solid interface in a sample that showed flow at 50 mK.

the solid. With our post-docs Ryosuke Ishiguro and Satoshi Sasaki, we performed a Torricellian experiment with solid helium [C6, C7]. We used an inverted test tube (10 mm diameter) with the top of the tube closed, and the bottom dipped in solid helium but kept 8 mm above the bottom of the cell (Fig. 1.3). We managed to have a level difference h between the liquid-solid interface inside and outside the tube. We observed that, in good quality crystals at 50 mK, h remained constant within 50 μm over 4 hours, corresponding to v at least 300 times less than what one would expect from the torsional oscillator results. However, in two lower quality crystals with GBs (as revealed by the presence of cusps at the liquid-solid interface), flow did occur at 50 mK (Fig. 1.3), with a different but constant velocity in each crystal, which is characteristic of superflow. If one assumes that GBs with a few atomic layers thickness are superfluid, this would correspond to a critical velocity v_c of a few $\mathrm{m\,s^{-1}}$. A similar value was measured in liquid films of atomic thickness [10]. Finally, in a third crystal with many cusps, we observed a similar superflow at 1.13 K, suggesting that a GB could be thick enough to exhibit a high critical temperature. We decided to investigate more closely the behavior of a single GB, as explained above.

Our findings about the wetting properties of GBs question the interpretation of our DC flow experiments: the flow in the test tube requires a GB, but it could take place either along the GB, or along the two liquid channels it makes on the tube walls according to Sec. 1.1.1. In the latter case, taking 870 $\mu\mathrm{m}^2$ for the cross section area of a channel at a depth $z = 10$ mm below the free liquid-solid interface [C2], we find a critical velocity $v_c \simeq 3\,\mathrm{ms^{-1}}$ along the channel. This is a reasonable value for this channel size [11]. If mass was really transported along these channels, it would explain why relaxation took place at least up to 1.1 K while GBs are predicted to become superfluid only around 0.5 K [4]. Measurements in different cell geometries are required in order to decide which mechanism is relevant. It would also be interesting to study the temperature dependence in detail.

Another experiment has found DC flow through the solid [12], but off the melting curve, in contrast to our experiment. The flow was observed to exist at low temperature, and to disappear upon heating above 500 mK. As at that time the flow was not seen to reappear upon cooling, we proposed [C8] that it could be due to liquid channels that exist inside the solid at the junction between 3 GBs [C2]. However, subsequent

runs showed an example of flow disappearing upon warming and reappearing upon cooling [13]. There are many other issues related to supersolidity [C5], but they fall beyond the scope of this report.

1.2 Capillarity in nanopores

A consequence of capillary is the displacement of phase equilibrium for a curved interface. This leads to the phenomenon of *capillary condensation*: a vapor will condense within small pores before its pressure reaches the saturated vapor pressure. In addition, an hysteresis has been noticed between condensation and desorption: to start emptying the pore, the pressure of the vapor has to be reduced below the value for condensation. Much work has been devoted to this issue and our contribution is modest. Nevertheless, we find it interesting to report in the next section our discussion of recent papers in this field. Then we will revisit the early problem of capillary rise, and discuss how the classical laws which apply to small but still macroscopic pores have to be modified to describe pores at the nanoscale.

1.2.1 Capillary condensation

Condensation in a cylindrical nanopore

The equilibrium vapor pressure for a liquid-vapor interface with curvature C is given by the classical Kelvin equation [1]:

$$P_{\rm eq} = P_{\rm sat} \exp\left(-\frac{\sigma V C}{RT}\right), \tag{1.8}$$

where $P_{\rm sat}$ is the saturated vapor pressure (i.e. the equilibrium pressure for a flat interface), σ the surface tension, and V the molar volume of the liquid.[3] This equilibrium is stable if the curvature is positive.

The simplest explanation of the hysteresis between adsorption and desorption is due to Cohan in 1938 [14]. It is based on the identification of the two possible states for a liquid in a pore: adsorbed as a film along the pore walls (Fig. 1.4 (a)), or condensed so as to form a bridge connecting the walls of the pores (Fig. 1.4 (b)). For a cylindrical pore of radius R, the film state is an annular film with a curvature $C > 1/R$, whereas the condensed state exhibits hemispherical menisci with a total curvature $2/R$ in case of complete wetting (zero contact angle). Eq. 1.8 thus explains the difference between adsorption and desorption pressures ($P_{\rm A}$ and $P_{\rm D}$, respectively). They satisfy the relation ${P_{\rm A}}^2 = P_{\rm sat} P_{\rm D}$. For a slit pore (the space between two flat walls) of thickness d, $P_{\rm A} = P_{\rm sat}$ and $P_{\rm D}$ is given by Eq. 1.8 with $C = 1/d$.

This simple model does not explain why the film state forms: for vapor pressures less than that given by Eq. 1.8 when $C = 1/R$, the pore should be completely dry, with no liquid at all. Sometimes an *ad hoc* film thickness is introduced, to match the measured value of $P_{\rm A}$ so that $C = 1/(R-t)$. To improve the description, one has to consider the interaction between the adsorbate and the pore walls. This has been done by Cole and Saam [15,16]. The interaction with the pore walls results in an additional term $U(z)$ in the chemical potential of the fluid, where z is the shortest distance to the wall. For a plane surface and non-retarded interaction forces:

$$U(z) = -\frac{A}{6\pi V z^3}, \tag{1.9}$$

[3] We use the convention of positive curvature ($C > 0$) when the liquid is on the *convex* side.

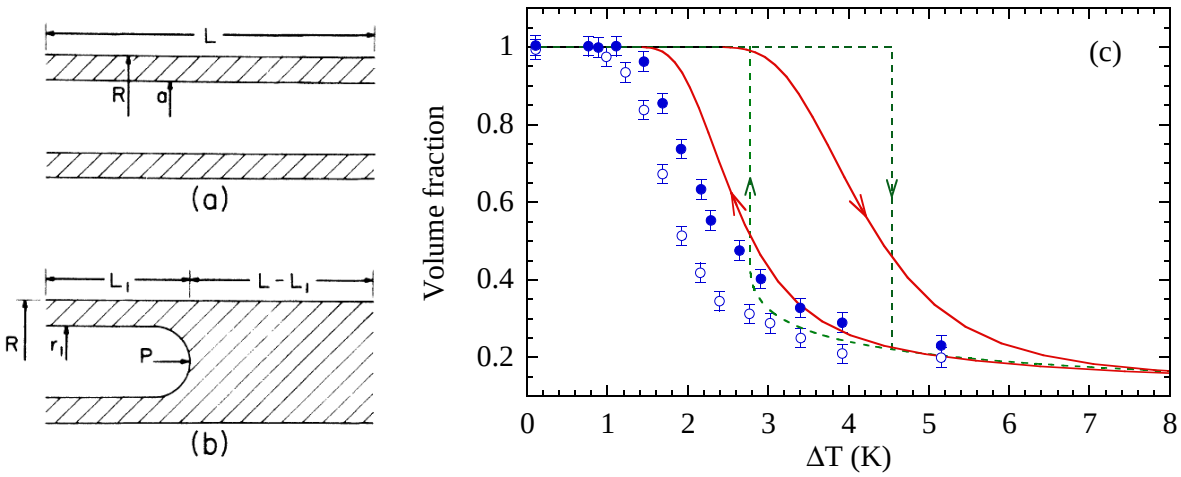

Figure 1.4: Possible states of a fluid adsorbed in a nanopore: film state (a) and condensed state (b). (c) Comparison of adsorption (○) and desorption (●) data [17] with CST for a single pore radius $R = 11.8\,\mathrm{nm}$ (dashed curves), and a gaussian distribution of pore radii (average $R = 11.8\,\mathrm{nm}$, rms deviation 2.5 nm) (solid curves).

where A is the Hamaker constant for the interacting system. The confined geometry in a cylindrical pore reinforces the interaction and leads to a modified expression for $U(z)$. We refer the reader to Ref. [16] for full details. This additional term explains why the denser phase creates a film, even at low vapor pressures. The full adsorption-desorption curve can now be predicted, including the values of P_A and P_D. When, during filling, the pressure is increased between P_D and P_A, the condensed state is the most stable one, but it does not form because it would require a large fluctuation to form the capillary bridge from the film state; instead the film continues to grow in metastable equilibrium with the vapor, until it becomes unstable at a pressure P_A. The pore is then filled with liquid with menisci at both ends, whose curvature depends on the vapor pressure. When the vapor pressure is decreased and reaches P_D, the menisci recede inside the pore, leaving a film in equilibrium with the vapor and the condensed state.

Numerous studies of capillary condensation have been performed over the last decades. To obtain pores with a small diameter, the early studies had to rely on disordered porous materials made of networks of tortuous, interconnected pores will variable size and shape. Recently, the advent of efficient synthesis techniques has allowed the production of assemblies of independent, straight, and cylindrical pores, which render the comparison with theory more direct. Nanoporous alumina is one of the new well-defined substrate available; it consists in a parallel arrangement of cylindrical pores around 20 nm in diameter, with a very large aspect ratio (1:5000). Alvine *et al.* [17] have used such a system to study adsorption-desorption of a solvent (perfluoromethylcyclohexane) at room temperature. They observed the usual hysteretic transition, and argued that its width (0.4 K) was five times smaller than the prediction by Cohan [14] (1.9 K), and that the data agree better with Cole and Saam theory (CST) [15, 16]. However, we have shown that they made only a partial comparison with CST [C9]. Adsorption is usually measured at constant temperature T by increasing the pressure P of a vapor from 0 to the saturated vapor pressure $P_\mathrm{sat}(T)$. CST calculates the liquid volume fraction V as a function of $p = P/P_\mathrm{sat}(T)$. Alvine *et al.* measure V as a function of the temperature offset ΔT between the porous sample at T_s and a liquid reservoir at T_r. They find that the volume fractions at the onset of filling (V_c) and the completion of emptying (V_m) compare well with the CST. However, according

to them, in CST, "there is no prediction of the ΔT where the desorption transition initiates [$\Delta T_{\rm m}$], and it is not possible to translate $V_{\rm c}$ and $V_{\rm m}$ into a hysteresis width." We have shown that it was in fact straightforward to express the results of CST with their experimental parameter, the temperature offset ΔT, instead of the usual reduced pressure $p = P/P_{\rm sat}(T)$ [C9]. Indeed, as $T_{\rm s}$ goes down to $T_{\rm r}$, p increases up to 1, and we can write a first integral of the Clausius-Clapeyron equation:

$$\Delta T = -(N_{\rm A} k_{\rm B} {T_{\rm r}}^2 / H_{\rm vap}) \ln p \,, \tag{1.10}$$

where $H_{\rm vap} = 33.9\,{\rm kJ\,mol^{-1}}$ [17] is the latent heat for vaporization, and where we have ignored the T-dependence of other parameters, as $\Delta T/T_{\rm r}$ is only a few percents. As can be seen on Fig. 1.4, the data do not agree with CST, even if the polydispersity of the pores is taken into account. We have suggested that a reason may be found in the existence of a hysteresis critical temperature $T_{\rm ch}$, at which hysteresis vanishes [18]. From the ratio between the molecular diameter of perfluoromethylcyclohexane and R, we estimate $T_{\rm ch} \simeq 430\,{\rm K}$, and $T_{\rm r}/T_{\rm ch} \simeq 0.71$.

Condensation near an AFM tip

Another type of pore is the one formed between two surfaces brought close together. Capillary condensation will occur most likely at the point where the distance between the surfaces is minimal, which depends on their geometries and on their asperities. The existence of capillary bridges will result in a strong attractive force between the surfaces, and is one of the aspects of the field of adhesion; see Ref. [19] for a recent review. A way to achieve a well controlled geometry is to use the sphere-plane system, which can be realized using the tip of an atomic force microscope (AFM) and a flat silicon wafer (Fig. 1.5 (a)). Such a system has been extensively studied, either with a sphere glued at the AFM tip, or directly with the AFM tip which is often approximated by a paraboloid. Recently, Yang *et al.* [20] have used the latter geometry to measure the pull-off force $F_{\rm po}$ needed to separate the surfaces as a function of the relative humidity, RH $= P_{\rm V}/P_{\rm sat}$. They decompose the pull-off force into the sum of two components of the capillary force (the Laplace force, $F_{\rm L}$, and the line tension force $F_{\rm T}$) and other forces $F_{\rm others}$ (van der Waals, chemical bonding, electrostatic...):

$$F_{\rm po} = F_{\rm L} + F_{\rm T} + F_{\rm others} \,. \tag{1.11}$$

Assuming that $F_{\rm others}$ is the same whether a liquid bridge is present or not, they identify the difference between the force at a given RH and that in ultrahigh vacuum (RH $= 0$) with the capillary force $F_{\rm cap} = F_{\rm L} + F_{\rm T}$ due to a water capillary bridge. Then they use a simple capillary model based on the Kelvin equation (Eq. 1.8) and the macroscopic contact angle of the liquid on the substrate to predict the curvature and the overall geometry of the bridge. Finally they calculate $F_{\rm T}$ and deduce the negative pressure inside the water $P_{\rm L} = -F_{\rm L}/A$ where A is the cross section area of the waist of the bridge. With this analysis, they obtain pressures as low as $-120 \pm 40\,{\rm MPa}$ (at RH $= 1\%$) inside the water in the bridge.

We have criticized this analysis [C10]. We have shown that, if the Kelvin equation held for their system, then it would lead *directly* to the value of the pressure inside the bridge; to first order:

$$P_{\rm L} = P_{\rm sat} + \frac{RT}{V_{\rm sat}} \ln({\rm RH}), \tag{1.12}$$

where $R = 8.3145\,{\rm J\,K^{-1}\,mol^{-1}}$ is the perfect gas constant, T the temperature, and $V_{\rm sat}$ the molar volume of the liquid at $P_{\rm sat}$. This formula leads to values markedly different

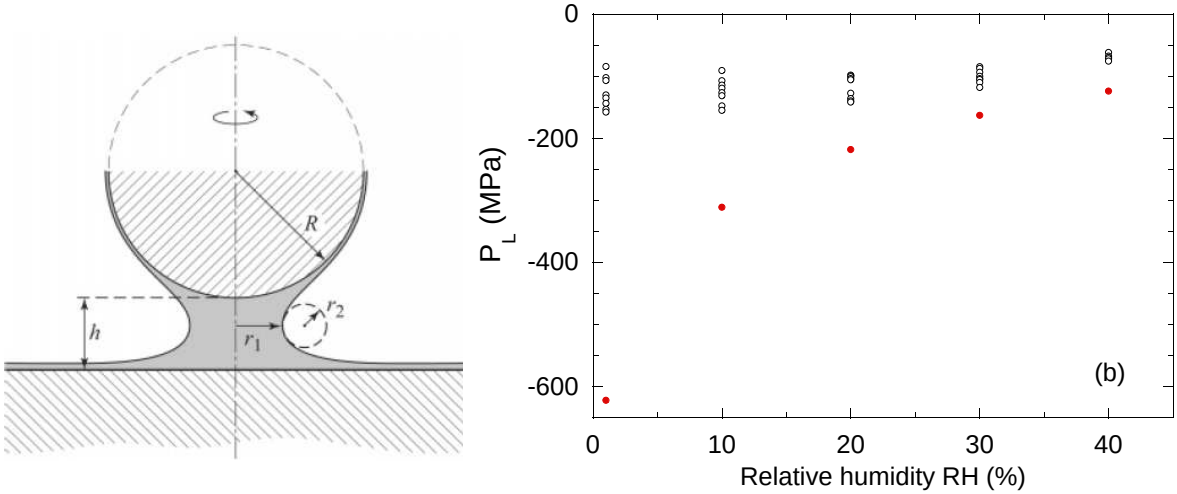

Figure 1.5: (a) Sketch of the liquid meniscus adsorbed between a spherical tip and a flat substrate. (b) Estimated pressure P_{L} inside the capillary bridge as a function of RH, based on the combination of pull-off force measurements and the Kelvin equation [20] (empty circles), and based on the Kelvin equation alone [C10] (full circles).

from those deduced from the above approach (Fig 1.5 (b)). We have proposed several explanations of this discrepancy [C10]. We cite here the two main problems with the above analysis. The assumption that F_{others} does not change with the presence of a liquid bridge is highly questionable: the dielectric properties of the medium between the surfaces screen the van der Waals force by an amount comparable to F_{cap} itself. However, this would lead to an even more negative pressure. The problem is that the most negative pressures are obtained for very low RH, at which the bridge becomes of molecular dimension. For a tip in contact with the wafer, using the same formulas as in Ref. [20], we find that the numerical value of the maximum thickness h of the liquid layer varies from 0.2 to 1 nm, for RH from 1% to 40%. This is to be compared with the size of a water molecule (around 0.3 nm), the thickness of a planar liquid-vapor interface (around 1 nm [C11]), and the wafer average roughness (0.4 nm [20]). The use of the contact angle θ of water on silicon taken from measurements on macroscopic drops, the description of the wafer as a flat surface, and the use of a simple capillary description (with a sharp water-vapor interface, the bulk surface tension σ and the Kelvin equation) are therefore highly questionable. In fact, for water confined to such small scales, the pressure itself is not defined as a scalar quantity: it is rather a non-diagonal stress tensor which includes the effect of water-water and water substrate interaction.

Consequences for the study of water

We have seen that the state of the confined liquid can be peculiar, and it is not always straightforward to describe it based on the sole knowledge of the outside control parameter such as the vapor pressure. In our opinion, this gives a caveat to the conclusions about the phase diagram of water that are drawn from measurements on the confined liquid. In a recent series of papers [21–26], the groups of Chen and Mallamace have been able to observed water at very low temperature in a state identified as liquid by confining it into narrow pores (less than 2 nm in diameter). Crystallization can then be avoided because of the favorable wetting of the walls by the liquid. They have discovered interesting anomalies, such as the existence of a density *minimum*

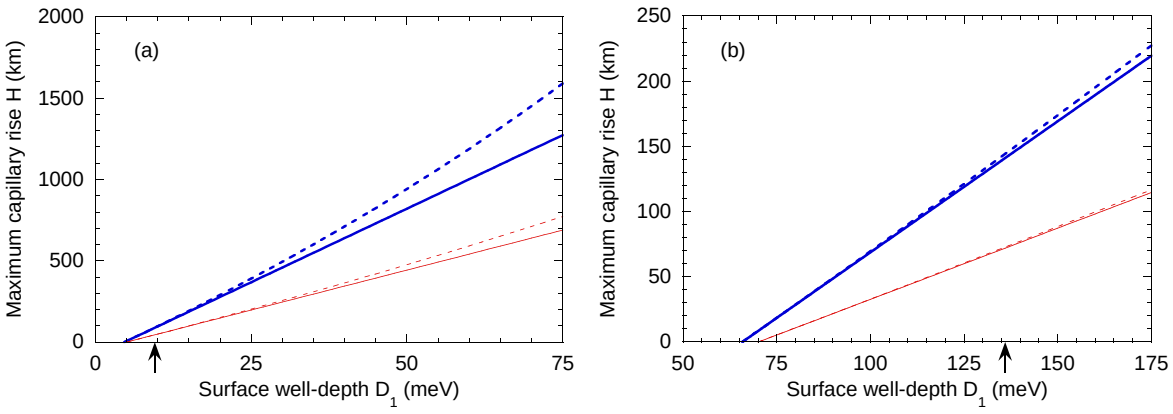

Figure 1.6: Capillary rise H as a function of well-depth D_1 of hydrogen H_2 (a) and water (b). Bold full and dashed curves denote the rise for a cylindrical pore without and with spherical Earth correction of the gravitational field, respectively. Lighter curves represent results for the slit pore case. The arrow indicates the threshold for wetting on a flat surface [C12].

around 210°C for D_2O [23] and 203°C for H_2O [25]. These anomalies could be evidence for the crossing of the Widom line emanating from a *liquid-liquid* critical point in the supercooled region; more details will be given in Sec. 2.2.1. Here we note that, in the first experiments, the pores were filled at a pressure somewhere above but close to the capillary filling transition. This suggests that the actual pressure in the liquid is negative, because of the meniscus curvature. However, the small dimensions make the direct use of Laplace's law uncertain, and the interaction with the walls may in fact result in a non diagonal pressure tensor. In experiments using helium gas as a transmitting pressure medium, the anomalies vanish above a helium pressure of around 150 MPa [23], but we think that the pressure of the liquid remains to be determined.

1.2.2 Capillary rise

The history of capillarity begins with the observation that liquids can rise inside a narrow tube. The physical law that predicts the height of this capillary rise is Jurin's law [1]. In the case of a perfectly wet cylindrical tube of radius R,

$$H_{\rm macro} = \frac{2\gamma}{\rho g R}\,, \tag{1.13}$$

where $g = 9.81\,{\rm m\,s^{-2}}$ is the gravitational acceleration. One is thus tempted to use as narrow a capillary as possible to achieve a maximal rise. For example, the formula yields $H_{\rm macro} \simeq 30\,{\rm km}$ for the case of water at 20°C and $R = 0.5\,{\rm nm}$. Beyond the problem of experimentally realizing such long capillaries (to which we come back later), the use of a law based on a macroscopic capillary model is questionable at the nanoscale. During his visit to our group, Milton W. Cole (Penn State Univ.) had the idea to resort to a first principle analysis to give the nanoscopic counterpart of Jurin's law [C12]. We write that the gravitational energy lost during the rise must be compensated by the binding energy gained when transferring a fluid particle from the bulk to the confined space in the pore:

$$MgH = E - E_{\rm bulk}\,. \tag{1.14}$$

We have considered Lennard-Jones (6-12) interactions, and two pore geometries (slit and cylinder). The size of the pore can be optimized to give the strongest binding

E [27]. We have calculated the rise for a series of adsorbates confined in graphite and MgO. It depends on the well depth D_1 of the attraction between the adsorbate and the substrate; the examples of hydrogen and water are given on Fig. 1.6. Imbibition occurs if D_1 exceeds a threshold value. We found that it is lower than that for wetting on a flat surface. This is a consequence of the enhanced substrate attraction in the pore compared to the single planar surface. The largest rise would be 857 km, obtained for hydrogen confined in a graphite tube with a radius of 0.277 nm; at these heights one would even have to consider a correction to Earth's gravity! Of course, such values seem completely out of reach. Even if such tremendously tall capillaries could be realized, we have estimated from the Lucas-Washburn equation [1] that it would take around $5\,10^9$ years to fill a capillary of radius 1 nm with water at 20°C! Nevertheless, we still think that an experimental test could be performed. The trick would be to use an ultracentrifuge to increase g to an apparent value which could be around $N = 4.8\,10^5$ times as large with a commercially available apparatus. The actual rise would then be divided by N and the time required for filling by N^2. A rise of a few centimeters in a porous glass like Vycor could then be measured.

1.3 Density functional theory of interfaces

The simplest approach to interfacial phenomena is the capillary approximation. It consists in neglecting the thickness of the interface separating two phases. The system can then be described as two subsystems identical to the bulk phases, and an interfacial part carrying an extra free energy σ per unit surface, where σ is the interfacial tension. This energy arises from the different environment experienced by the particles near the interface compared to the bulk ones. This approach is an approximation, because the interfacial region is not atomically sharp. In Sec. 1.3.1 we describe a more elaborate theory, which we apply to the liquid-vapor interface of water in Sec. 1.3.2 and to the liquid-solid interface of helium in Sec 1.3.3.

1.3.1 Density functional formalism

For a one component system, the coexistence of two phases with different densities in a system with fixed temperature, volume, and number of particles, will lead to an interfacial density profile $\rho(z)$, where z is a coordinate along the direction perpendicular to the interface. The free energy per unit volume of the substance varies with density. By definition, the two coexisting phases have the same, lowest free energy. This implies that the intermediate densities explored by the interfacial profile give rise to an excess free energy. This excess energy could be reduced to zero by making the interface infinitely thin; however, such a sharp density jump is not allowed at the atomic scale: inhomogeneities in the local average density are energetically costly. To describe the competition between these two contributions, Cahn and Hilliard have introduced the concept of *density functional theory* (DFT) [28]; the idea can be traced back to Van der Waals' thesis. The free energy F of the system is a function of the function $\rho(\mathbf{r})$ describing the profile - hence the term *functional*. The simplest version is called the *square gradient approximation*:

$$F[\rho] = \int \mathrm{d}^3\mathbf{r}\ \left[f\left(\rho(\mathbf{r})\right) + \lambda \left(\nabla\rho(\mathbf{r})\right)^2 \right], \tag{1.15}$$

where f is the free energy per unit volume, and λ a parameter. One can use the rules of variational calculation to solve for the optimum profile at equilibrium [28].

To enforce the condition of mass conservation, we introduce a Lagrange multiplier μ, and minimize the quantity $F - \mu N$ where $N = \int \mathrm{d}^3\mathbf{r}\, \rho(\mathbf{r})$ is the total number of particles. It is easily shown that, if the system contains homogeneous regions at different densities, μ is the common chemical potential at coexistence, and $F - \mu N$ is thus the grand potential. For a planar interface across the z direction separating two phases at densities ρ_1 and ρ_2, the solution is conveniently written in the form:

$$z(\rho) = \int_{\rho}^{\rho(z=0)} \sqrt{\frac{\lambda}{\phi(\rho)}}\, \mathrm{d}\rho\,, \tag{1.16}$$

where $\phi(\rho) = f(\rho) - f(\rho_1) - \mu(\rho - \rho_1)$. We get now to the key point that, combining Eqs. 1.15 and 1.16, DFT gives a formula for the interfacial tension:

$$\sigma = 2\int_{\rho_1}^{\rho_2} \sqrt{\lambda\phi(\rho)}\, \mathrm{d}\rho\,. \tag{1.17}$$

With the input of the function f and the value of σ, Eq. 1.17 shows how the value of the parameter λ can be adjusted. DFT now becomes *predictive*, as it provides the shape of the interface (Eq. 1.16) and in particular its thickness, which can be compared to an independent determination.

We will now explain how we have used this approach to describe the liquid-vapor interface of water (Sec. 1.3.2) [C11], and a modified quantum version for the case of the liquid-solid interface of helium (Sec. 1.3.3) [C13–C16].

1.3.2 Liquid-vapor interface of water

In Ref. [C11], we use the DFT formalism introduced in Sec. 1.3.1 to treat the specific case of the liquid-vapor interface of water. We need as input the free energy per unit volume f and the surface tension σ. For the latter, we use the IAPWS formula [29] that reproduces the experimental values from the triple point to the critical point. For the former, we need the equation of state (EoS), but we cannot simply use the experimental data, because they are available only in the *stable* phases: if ρ_v and ρ_l are the vapor and liquid density at coexistence, respectively, the data is missing for $\rho_\mathrm{v} < \rho < \rho_\mathrm{l}$. It could be measured in principle in the metastable states, but certainly not in the density range lying between the liquid-vapor and vapor-liquid spinodals[4]. We have therefore to rely on an extrapolation. To extrapolate from the liquid side, we have used the simple, yet accurate form of the EoS proposed by Speedy [30]:

$$1 - \frac{P}{P_\mathrm{S}(T)} = B(T)\left(\frac{\rho}{\rho_\mathrm{s}(T)} - 1\right)^2, \tag{1.18}$$

with three adjustable parameters: B, and P_S and ρ_s which are the liquid-vapor spinodal pressure and density, respectively. Eq. 1.18 can be integrated to find f for $\rho \geq \rho_\mathrm{s}$:

$$f(\rho) = \frac{\rho}{\rho_0}\, f(\rho_0) + \rho \int_{\rho_0}^{\rho} \frac{P(\rho')}{\rho'^2}\, \mathrm{d}\rho', \tag{1.19}$$

where $\rho_0 \geq \rho_\mathrm{s}$ is a reference density (e.g. $\rho_0 = \rho_\mathrm{l}$); the constant $f(\rho_0)$ can be chosen arbitrarily and cancels out in the results. To determine f for $0 \leq \rho \leq \rho_\mathrm{s}$, we have then used two different interpolation schemes, see Ref. [C11] for details.

[4]Section 2.1.2 will recall the definition of a spinodal line and discuss its importance in water and helium.

The motivation of the work was actually to compare two EoS for water with a qualitatively different behavior. They correspond to two completely different scenarios to explain the anomalies of supercooled water. We postpone the description of these scenarios to Sec. 2.2.1. At this stage, we just want to mention the following features. The EoS was obtained in one case by a fit with Eq. 1.18 using experimental data only, while we derived the other by fitting results of molecular dynamics simulations. The resulting liquid-vapor spinodal are qualitatively different: the former gives a minimum in the spinodal pressure around 310 K, and the latter gives a spinodal pressure increasing monotonically with temperature. As the interfacial profile explores densities in the vicinity of the spinodal, we expected that the different qualitative behaviors would show up in the variation of the interfacial thickness with temperature. That this is indeed the case can be seen on Fig. 1.7. The temperature variation of the spinodal pressure is reflected in the prediction for l_{10-90}:

$$l_{10-90} = \int_{0.9\rho_\mathrm{v}+0.1\rho_\mathrm{l}}^{0.1\rho_\mathrm{v}+0.9\rho_\mathrm{l}} \sqrt{\frac{\lambda}{\phi(\rho,\rho_\mathrm{l})}}\,\mathrm{d}\rho\,. \tag{1.20}$$

Although the absolute value of l_{10-90} depends on the choice of the extrapolation, the temperature dependence does not. The comparison with experimental data favors the monotonic spinodal. However, we would like to emphasize that the ellipsometry data shown on Fig. 1.7 gives a larger l_{10-90} than many other ellipsometry measurements, available only at room temperature, which give around 0.4 nm. The test is not fully conclusive. A more direct way to approach the spinodal is to study directly the metastable liquid, at a pressure below the saturated vapor pressure. This route will be discussed theoretically in Chapter 2 and experimentally in Chapter 3.

1.3.3 Liquid-solid interface of helium

DFT can be extended to describe the liquid-solid interface. The idea of the Ramakrishnan-Yussouff method (RY) [31, 32] is to treat the solid as a spatially periodic perturbation (density $\rho_\mathrm{s}(\mathbf{r})$) of the uniform liquid (density ρ_l). The difference in energy between both phases is obtained by a Taylor expansion truncated to second order:

$$\Delta E[\rho] = E_\mathrm{id}[\rho] + \int \mathrm{d}\mathbf{r} \left(\frac{\delta E_\mathrm{int}}{\delta\rho(\mathbf{r})}\right)_\mathrm{l} \delta\rho(\mathbf{r}) + \frac{1}{2}\int \mathrm{d}\mathbf{r}\mathrm{d}\mathbf{r}' \left(\frac{\delta^2 E_\mathrm{int}}{\delta\rho(\mathbf{r})\delta\rho(\mathbf{r}')}\right)_\mathrm{l} \delta\rho(\mathbf{r})\delta\rho(\mathbf{r}'), \tag{1.21}$$

with $\delta\rho(\mathbf{r}) = \rho_\mathrm{s}(\mathbf{r}) - \rho_\mathrm{l}$, E_id the energy of the noninteracting inhomogeneous system and E_int the interacting part of the energy. The quantum version of RY is described in Refs. [33, 34]. For Bose particles of mass m, E_id is the kinetic energy:

$$E_\mathrm{id} = \frac{\hbar^2}{2m}\int \mathrm{d}\mathbf{r} \left\{\nabla\left[\sqrt{\rho(\mathbf{r})}\right]\right\}^2. \tag{1.22}$$

The second term on the right hand side of Eq. 1.21 is the mass term: the derivative of E_int is the chemical potential μ_l of the liquid. The third term involves the direct correlation function (DCF)

$$\left(\frac{\delta^2 E_\mathrm{int}}{\delta\rho(\mathbf{r})\delta\rho(\mathbf{r}')}\right)_\mathrm{l} = v(|\mathbf{r}-\mathbf{r}'|;\rho_\mathrm{l}), \tag{1.23}$$

which is the quantum analog of the classical Ornstein-Zernike DCF. Dealing with a periodic density, the calculations are more conveniently carried out in Fourier space;

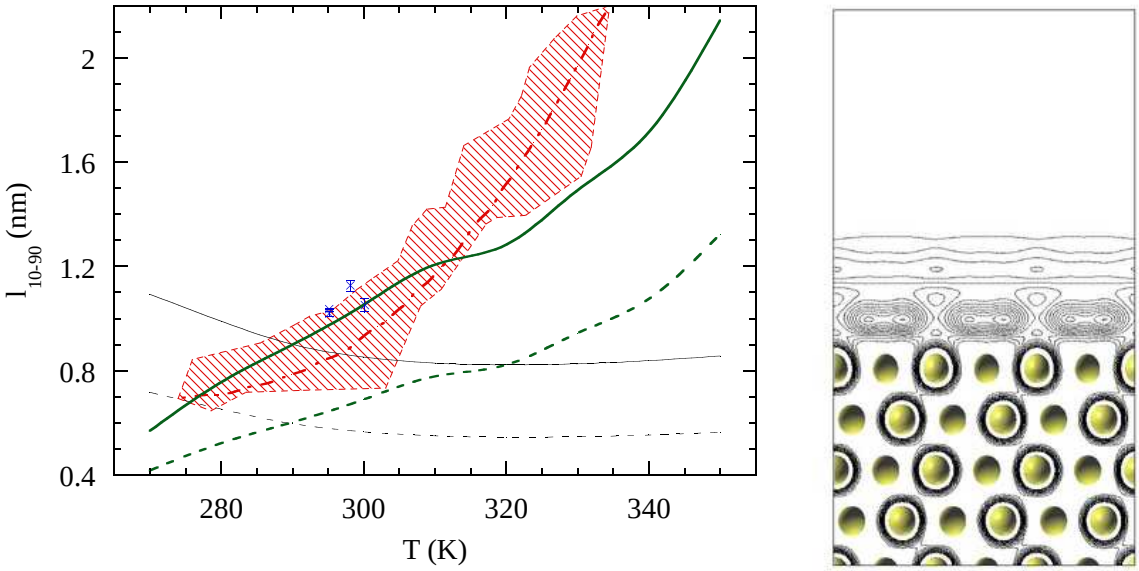

Figure 1.7: *Left*: 10-90 % thickness of the liquid-vapor interface of water vs. temperature [C11]. The thin and thick lines were calculated using the EoS with a minimum in the spinodal and with a monotonic spinodal, respectively. The solid and dashed lines corresponds to the two extrapolations used for $f(\rho)$. The thick dash-dotted line shows ellipsometry measurements (the hatched area indicates the scatter of the data). The crosses (with error bars) show the values derived from several x-ray scattering experiments. The corresponding references are given in Ref. [C11]. *Right*: Liquid-solid interface of helium 4 predicted by DFT [C15], shown by means of equal density contour lines (drawn between $\rho = 0.02$ Å^{-3} and $\rho = 0.05$ Å^{-3}) in a plane perpendicular to the interface plane. Constant density surfaces (at $\rho = 0.08$ Å^{-3}) are also shown to identify the atoms in the solid slab.

the Fourier transform of v is related to the static linear response function χ of the liquid:

$$v(q;\rho_l) = \frac{1}{\chi_0(q)} - \frac{1}{\chi(q)}\,, \tag{1.24}$$

where χ_0 is the non-interacting limit: $\chi_0(q) = -(4m\rho_l)/(\hbar^2 q^2)$.

To find equilibrium one usually considers the grand-canonical system. Choosing a liquid density ρ_l in a fixed volume V at zero temperature, one finds the most stable solid at the same chemical potential $\mu = \mu_l$ by minimizing the grand-potential difference $\Delta\Omega = \Delta E - \mu V(\rho_s - \rho_l)$. The minimum in $\Delta\Omega$ results from the competition between the interaction term in Eq. 1.21, which favors localization, and the kinetic term which tends to homogenize the system. Instead of performing the full minimization, one usually resorts to a variational approach, parameterizing the solid by gaussians centered at the lattice sites [33, 34]. The fcc lattice is usually chosen, although helium actually freezes into hcp at zero temperature; fcc is easier to handle, and the two symmetries were found to give scarcely distinct results [35].

We have followed the variational minimization procedure [C13], using as an input for χ the formulation provided by the Orsay-Trento functional [36], a DFT based on a hamiltonian description of superfluid helium, with parameters fitted to reproduce many experimental properties, including χ at the saturated vapor pressure, and its pressure dependence predicted by simulations. We find that the solid is always too stable. Then we have tried to rescale χ by a constant factor (0.9369), fitted to reproduce the experimental freezing density. With no more adjustable parameters, we were then able

to reproduce the experimental equation of state of the solid [C13].

We then tried to describe a flat interface extending perpendicularly to an axis $\hat{\mathbf{z}}$. This is possible within DFT of freezing, which is in principle able to predict the interfacial tension and the interfacial profile. The density profile can be written as:

$$\rho(\mathbf{r}) = \rho_{\mathrm{l}} \left[1 + \sum_j \mu_j(z)\, e^{\mathrm{i}\mathbf{k}_j \cdot \mathbf{r}} \right], \tag{1.25}$$

where the $\mathbf{k}_j$'s are the reciprocal lattice vectors (RLVs) and the order parameters μ_j vary through the interface, from the solid to the liquid values. The excess energy of the interface is again given by Eq. 1.21. When the μ_j's vary slowly on the distance between two atomic layers, their second order Taylor expansion may be used to calculate the interacting part; this is called the *square gradient approximation* (SGA) [37]. We have adapted SGA to the quantum case and tried to find a variationally optimized profile [C14]. We find an interfacial tension $\gamma = 0.47\,\mathrm{mJ\,m^{-2}}$ and a thickness of the interface $\xi = 0.56\,\mathrm{nm}$. We can compare to the experimental value $\gamma = 0.17\,\mathrm{mJ\,m^{-2}}$ [2], or to the results of variational Monte Carlo simulations: $\gamma = 0.25 \pm 0.1\,\mathrm{mJ\,m^{-2}}$ and $\xi = 1 - 1.25\,\mathrm{nm}$ [38]. Unfortunately, in our result, the interface extends over only 3 lattice planes, which is not enough to justify the SGA.

We finally turned to a full, non variational minimization [C15]. Most of the calculations were performed by Francesco Ancilotto, from the University of Padova, Italy, following a project which was initiated during our common visit to the group of Manuel Barranco, at the University of Barcelona. We had to introduce an *ad hoc* modification of the Orsay-Trento functional to obtain the experimental freezing values, using adjustable parameters to reproduce the experimental equation of state for the solid. Nevertheless, it was an interesting result that the simulations converged to the stable solid structure, even if the initial configuration used had not the correct lattice parameter. Within this frame, we could get some indication of the interfacial structure and energy ($\gamma = 0.1\,\mathrm{mJ\,m^{-2}}$ and $\xi = 0.93\,\mathrm{nm}$) (see Fig. 1.7), but the numerical convergence was too slow to provide accurate values.

We also note that we made a technical contribution by comparing the different minimization schemes [C16]. We concluded that the shortcoming of the RY method was due to the poor quality of the second order approximation, rather than to the use of isotropic variational functions.

Chapter 2

Theoretical limits of metastability

The existence of surface tension is characteristic of first order transitions: the interface between two phases of the same substance costs some energy. We have seen in Chapter 1 how this affects stable equilibrium properties. But it is also responsible for the phenomenon of *metastability*: a phase can be observed for a finite time outside its stability region. As already mentioned in the Introduction, the liquid can be cooled down below the line of liquid-solid equilibrium in a *supercooled* state, *metastable* with respect to the solid. Similarly, the liquid can be warmed up above the line of liquid-vapor equilibrium, in a *superheated* state, metastable with respect to the vapor; or equivalently, the liquid can be depressurized below the line of liquid-vapor equilibrium, even to negative pressure, to reach a metastable *stretched* state. The common explanation for these phenomena is that, even if the metastable phase has a lower energy, its nucleation also involves an energy cost due to the creation of an interface.

However, metastable states have a finite lifetime, which decreases when the distance to the equilibrium line increases. Eventually, there are limits to the metastability; some limits are absolute ones, based on strong thermodynamic conditions; some depend on the experimental conditions and involve kinetic aspects. We will discuss the theory of these limits in this chapter, first from a general point of view in Sec. 2.1. Then we will address the case of stretched water in Sec. 2.2, and make the connection with water anomalies. In Sec. 2.3.1 we will discuss the metastability of liquid helium, not only with respect to the vapor, but also with respect to the solid. We will finally consider in Sec. 2.4 the technologically relevant issue of melting and freezing of nanocrystals.

2.1 Theoretical background

When a substance is in a metastable state, it is by definition favorable to convert the particles of the substance from the metastable state to the stable one: this represents a gain in energy proportional to the volume. However, this phase transition involves an interface between both phases, which represents a cost in energy proportional to the surface. For a small nucleus of the new phase, the surface cost exceeds the volume gain, whereas the balance is reversed for a large enough nucleus. This leads to the existence of a *critical nucleus*, for which the maximum energy is realized, which represents an *energy barrier* for the nucleation of the new phase. A review of the fascinating field of metastability and nucleation is available in an excellent book [39]. Here we will focus on the features required to understand our work on water and helium. We will first give a simple quantitative theory of nucleation in Sec. 2.1.1. Then we will explain in Sec. 2.1.2 why the energy barrier is bound to vanish in some cases, before presenting in Sec. 2.1.3 a density functional approach to nucleation that includes this absolute limit of metastability.

2.1.1 Classical nucleation theory

A derivation of the classical nucleation theory (CNT) can be found in Refs. [39–41] for instance. Here we briefly present the case of a one component system, evolving at constant temperature T, pressure P, and number of particles. We assume that P is below the equilibrium pressure $P_{\rm eq}$ between two phases 1 and 2, so that phase 1 is metastable with respect to phase 2. Let us call σ the interfacial energy between both phases. CNT makes the capillary approximation which consists in treating the interface as infinitely thin, with an energy σ per unit surface. The minimum work required to form a volume V of phase 2 in phase 1 is given by the variation of the thermodynamic potential $\widetilde{G} = U - TS + PV$. For an isotropic σ, the minimum value will be reached for spherical nuclei of phase 2, at a pressure P_2 such that the chemical potential of the particles of phase 2 in the nucleus will be equal to that of phase 1 outside, determined by the pressure P. For instance, for incompressible phases, we have:

$$\Delta P = P - P_2 = \left(1 - \frac{\rho_2}{\rho_1}\right)(P - P_{\rm eq}), \tag{2.1}$$

where ρ_i is the density of phase i. The minimum work required as a function of the radius R of the nucleus is:

$$\widetilde{G} = \frac{4\pi R^3}{3}\Delta P + 4\pi R^2 \sigma. \tag{2.2}$$

It results from the competition between the gain in volume energy and the cost in surface energy when creating the nucleus. At a critical radius

$$R_{\rm c} = \frac{2\sigma}{\Delta P}\,, \tag{2.3}$$

$\widetilde{G}$ goes through a maximum

$$E_{\rm b} = \frac{16\pi\sigma^3}{3\Delta P^2}\,. \tag{2.4}$$

Nuclei with a radius less than $R_{\rm c}$ decay spontaneously, whereas those with a radius above $R_{\rm c}$ will grow. $E_{\rm b}$ is therefore the energy barrier which has to be overcome for nucleation to take place. This explains why the new phase does not appear immediately, and why the other phase can be metastable; as this requires the existence of a finite interfacial energy, this holds only for first-order transitions. Note that the calculation was made for a bulk, pure substance: this corresponds to the situation of *homogeneous* nucleation, which is an intrinsic property of the substance. In many experiments, the influence of a wall or an impurity can reduce $E_{\rm b}$, leading to *heterogeneous* nucleation. In most cases, nucleation is a stochastic phenomenon. It will occur at a rate Γ per unit volume and time. Γ is related to $E_{\rm b}$ through a Boltzmann law:

$$\Gamma = \Gamma_0 \exp\left(-\frac{E_{\rm b}}{k_{\rm B}T}\right), \tag{2.5}$$

where Γ_0 is a prefactor. It can be determined from microscopic parameters in the case of nucleation of a liquid in a supersaturated vapor [39], but its value for other transitions is more ambiguous. We usually write Γ_0 as the product of a thermal frequency by the density of independent critical nuclei:

$$\Gamma_0 \simeq \frac{k_{\rm B}T}{h}\left(\frac{4}{3}\pi {R_{\rm c}}^3\right)^{-1}, \tag{2.6}$$

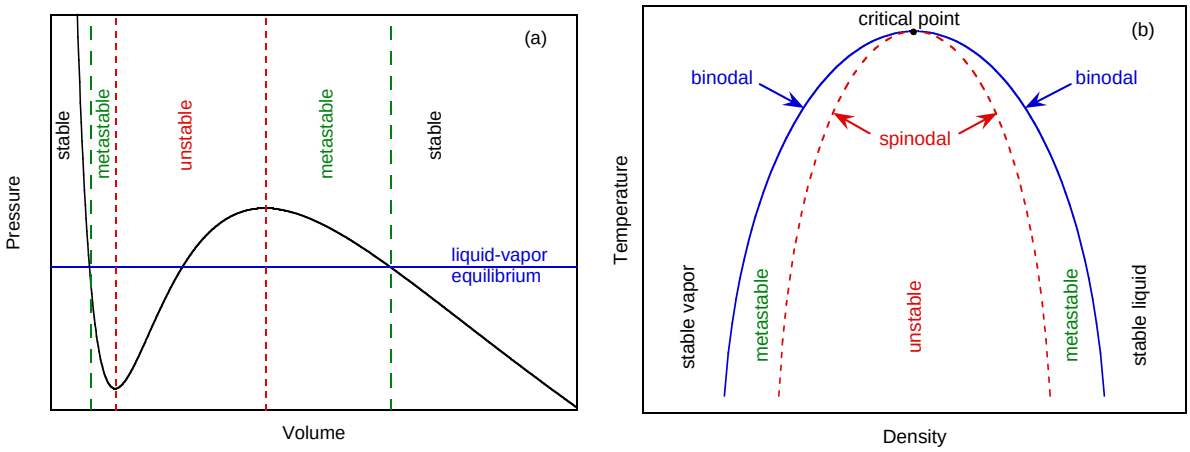

Figure 2.1: (a) Pressure as a function of volume, showing the regions where the fluid is stable, metastable, and unstable. (b) Sketch of a phase diagram with the liquid-vapor equilibrium (binodal) and the corresponding spinodals.

where h is Planck's constant. For an experiment performed in a volume V and during a time τ, the cavitation probability is $\Sigma = 1 - \exp(-\Gamma V \tau)$, and reaches $\frac{1}{2}$ when

$$\Gamma_0 V \tau \exp\left(-\frac{E_\mathrm{b}}{k_\mathrm{B} T}\right) = \ln 2. \tag{2.7}$$

This equation shows that the nucleation threshold is essentially determined by E_b. It reduces the importance of large uncertainties in Γ_0 or of large variations in $V\tau$ between experiments. In the case of cavitation (nucleation of the vapor in the metastable liquid at $P < P_\mathrm{sat}$, the saturated vapor pressure), $P_\mathrm{sat} - P_2 \ll |P|$ and the cavitation pressure is:

$$P_\mathrm{cav} = P_\mathrm{sat} - \left(\frac{16\pi\sigma^3}{3\,k_\mathrm{B}T}\,\frac{1}{\ln(\Gamma_0 V\tau/\ln 2)}\right)^{1/2}. \tag{2.8}$$

2.1.2 Spinodal limits

In the case of the nucleation of the vapor in a metastable liquid, CNT predicts that the energy barrier scales as the inverse of $(P - P_\mathrm{sat})^2$ (Eq. 2.4), and therefore never vanishes, even for infinitely negative pressure. However, this picture seems rather unphysical, because if the degree of stretching increases without limit, the particles will eventually explore separations beyond the inflexion point in the tail of the interparticle potential, which are unstable from a mechanical point of view. From a thermodynamic point of view, it corresponds to a region of low density where the free energy F of the liquid would be a concave function, which is forbidden by the second principle. Equivalently, as $P = -(\partial F/\partial V)_T$, it corresponds to a positive value of $(\partial P/\partial V)_T$ (Fig. 2.1 (a)). The locus of points where $(\partial P/\partial V)_T$ vanishes, i.e. the compressibility diverges, is called a *spinodal limit*. For the liquid-vapor transition, at temperatures below the critical point, two spinodal limits exist (Fig. 2.1 (b)): one for the transition from the liquid to the vapor and one from the vapor to the liquid. On the spinodal limit, the fluid becomes macroscopically unstable, and long wavelengths fluctuations can grow spontaneously, resulting in spinodal decomposition of the system. This is obviously not accounted for in CNT, and we present in the next section an improved theoretical approach.

2.1.3 Density functional theory of nucleation

The reason for the failure of CNT is that, at large degrees of metastability, the critical nucleus becomes very small: for cavitation, R_c scales as the inverse of ΔP (Eq. 2.3). Yet CNT treats the interface between both phases as a sharp wall with zero width, an approximation which fails when the critical nucleus is comparable in size to the interfacial thickness. One way to improve the theory is to resort to density functional theory (DFT), already introduced in Sec. 1.3. DFT can treat inhomogeneous systems, providing the free energy of a density profile. In nucleation theory, by allowing the interface to have a finite width, the free energy will be reduced. For a given point of the metastable region, DFT provides the optimal spherical profile that minimizes the energy barrier, and connects a low density region at the center to a region at the metastable density outside. One has to solve the Euler-Lagrange equation:

$$2\lambda\,\Delta\rho = \frac{\partial\phi}{\partial\rho}\,. \tag{2.9}$$

The notations are defined in Sec. 1.3.1. From the optimal profile, the energy barrier is calculated, and the nucleation rate follows as in Sec. 2.1.1. Because DFT is based on the specification of the free energy, it has the spinodal limits "built in". For the metastable liquid, as the density is reduced, the core of the critical nucleus becomes denser and denser, and when the spinodal density is approached, the profile becomes very shallow with a large radius, leading to a vanishing energy barrier, in contrast to CNT. On the other hand, when the system is close to equilibrium, the profile is very sharp, and ignoring the interfacial thickness becomes a good approximation: DFT and CNT approach each other asymptotically. We will use DFT to study cavitation in water in Sec. 2.2.2.

2.2 Stretched water

We now turn to the specific case of water at negative pressure, in a stretched state. We first review in Sec. 2.2.1 the different predictions that have been proposed for its liquid-vapor spinodal, and its relation to water anomalies. We then explain in Sec. 2.2.2 how these different predictions for the spinodal translate into qualitatively different cavitation limits that could be in principle checked experimentally.

2.2.1 Competing scenarios

The location of the liquid-vapor spinodal is well defined theoretically, as the line where the compressibility of the liquid diverges. However, its experimental determination is not straightforward, as measurements are difficult to perform in the metastable region. Consequently, one has often to rely on extrapolation of data measured in the stable region. This was done by Speedy for water [30]. He noticed that experimental isotherms [42] were accurately represented by the 3-parameters formula:

$$1 - \frac{P}{P_s(T)} = B(T)\left(\frac{\rho}{\rho_s(T)} - 1\right)^2. \tag{2.10}$$

This is the simplest functional form expected from a Taylor expansion in density from the spinodal point, and reproduces surprisingly well the data at positive pressure. The striking result is that the spinodal line $P_s(T)$ exhibits a minimum. Speedy gave an

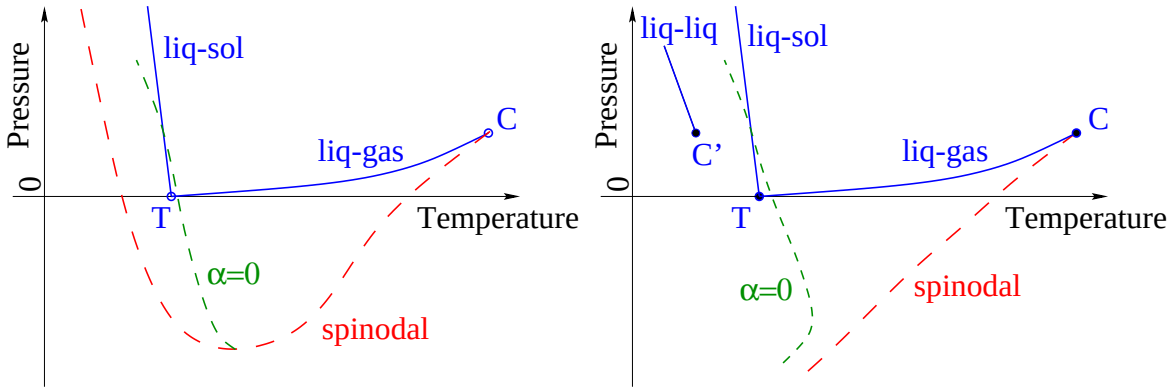

Figure 2.2: Sketch of the phase diagram of water illustrating two scenarios proposed to explain its anomalies. *Left*: Reentrant spinodal scenario [30]: the line of density maxima of water reaches the spinodal, which turns back to positive pressure and creates a line of instability where water properties diverge. *Right*: Second critical point scenario [47]: the line of density maxima avoids the spinodal which remains monotonic; the anomalies are explained by the proximity of a critical point ending a first-order transition between two liquid phases.

interesting physical explanation for the existence of this minimum. He showed that, if a line of density maxima intersects a spinodal line, the latter has to change slope (Figs. 2.2 (a)). Extrapolation of the line of density maxima measured in water at positive pressure suggests that this is the case and explains the minimum in $P_s(T)$. Speedy carries on the argument by proposing that the spinodal retraces to positive pressures, where it would become a line of instability for the supercooled liquid [30,43]. The nature of this line is not clear, and its thermodynamic consistency has been debated [44–46]. Nevertheless, Speedy's scenario is attractive as it could explain the divergence of many properties of liquid water when approaching the spinodal limit. Moreover, it might be that a minimum in $P_s(T)$ exists, while the spinodal does not retrace up to positive pressure.

On the other hand, molecular dynamic simulations of water disagree with Speedy's scenario. Simulations are based on a microscopic interaction potential, whose parameters are fitted to reproduce some of water properties. Although none of them is able to reproduce quantitatively *all* the features of water, they are useful tools to explore highly metastable regions sometimes inaccessible to the experiments. Some of them have been used to calculate isotherms, including a metastable part. The simulation data can be extrapolated using Eq. 2.10 to find the corresponding spinodal. This leads to a monotonic $P_s(T)$, while the line of density maxima reaches a maximum temperature and then changes slope to avoid the spinodal, thus satisfying thermodynamic consistency (Figs. 2.2 (b)) [47]. In all the simulations, the supercooled liquid does not exhibit a line of instability, but rather a liquid-liquid transition: it means that deeply supercooled water could exist in two distinct liquid phases with different structure. The transition between the low density liquid and the high density liquid is a first order transition, and it ends at a liquid-liquid critical point (LLCP). In this scenario, it is the LLCP that is responsible for the observed anomalies. Thermodynamic quantities can diverge only at the LLCP; however, they will show maximum values in its vicinity. The simulations predict that they will occur close to the Widom line, which is a line of correlation length maxima emanating from the LLCP.

For completeness, we note that other scenarios exist, but we will not develop them here, and we refer the reader to the reviews given in Refs. [44,48] and references therein. Our present purpose is to discuss if the distinct behavior of the spinodal curve $P_s(T)$

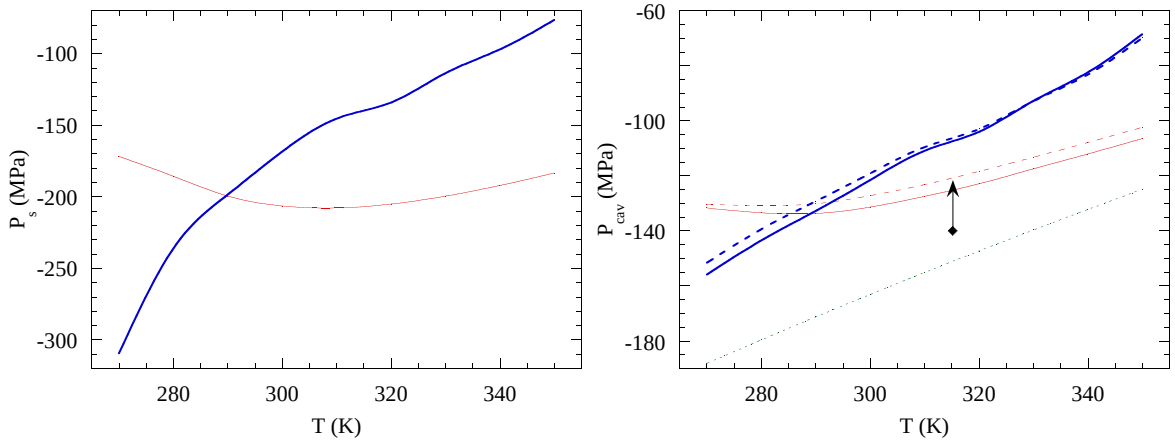

Figure 2.3: (a) Spinodal pressure vs. temperature. The thin (resp. thick) line is deduced from Speedy (resp. TIP5P) EoS. (b) Cavitation pressure vs. temperature. The dotted line shows the prediction of the CNT. The thin solid (resp. dashed) line was calculated using Speedy EoS, and the thick solid (resp. dashed) line using TIP5P EoS with our first (resp. second) extrapolation for $f(\rho)$. The filled diamond is the largest tension at which cavitation was observed in a quartz inclusion [49]; $P_{\rm cav}$ is calculated assuming that the volume of the inclusion remains constant; the arrow indicates the correction due to the matrix compliance effect.

predicted by each scenario could be observed experimentally. An experiment cannot reach the spinodal, because thermal fluctuations will trigger nucleation of the vapor phase before. Therefore, we decided to calculate the cavitation line associated with a typical example of each scenario.

2.2.2 Density functional predictions for cavitation

The classical nucleation theory ignores the existence of a liquid-vapor spinodal, and will therefore predict the same cavitation line for the different scenarios. In contrast, DFT has the liquid-vapor spinodal built-in through the equation of state. This is the reason why we decided to use DFT to predict the cavitation line [C11], choosing two equations of state representative of each of the two scenarios discussed above (Fig. 2.3 (a)). They are described in Sec. 1.3.2. We have seen in Sec. 1.3.1 how, for a given EoS, we can adjust the parameter λ involved in the square gradient approximation to fit the value of the surface tension. DFT then becomes predictive for the energy of any inhomogeneous density configuration. In particular, it can be used to find the critical nucleus that realizes the energy barrier $E_{\rm b}$ for nucleation of the vapor inside the metastable liquid [50]. We calculate $E_{\rm b}$ as a function of the liquid density, and from Eq. 2.4, we obtain the cavitation line. The results are shown on Fig. 2.3 (b). As expected, DFT predicts a less negative $P_{\rm cav}$ than CNT, but, more interestingly, the shape of the cavitation line reflects qualitatively that of the spinodal line: the EoS with a minimum in $P_{\rm s}(T)$ leads to a shallow minimum in $P_{\rm cav}(T)$, whereas the EoS with a monotonic $P_{\rm s}(T)$ leads to a monotonic $P_{\rm cav}(T)$.

This result motivated us to measure $P_{\rm cav}(T)$, with the hope to distinguish between the two competing scenarios. Our experimental work will be presented in Sec. 3.1. We anticipate by saying that we measured cavitation pressures much less negative than the DFT predictions. We propose different interpretations that will be described in Secs. 3.1.3 and 3.2.2.

2.3 Metastable helium

Liquid helium can also become metastable: with respect to the vapor, when it is stretched; and with respect to the solid, when it is overpressurized. We have reviewed our work in Refs. [C17–C19]. We present in Sec. 2.3.1 our conclusions on helium at negative pressure. We also consider overpressurized helium, describing our theoretical work on a possible liquid-solid spinodal (Sec. 2.3.2) and a theory for the nucleation of the solid that goes beyond CNT (Sec. 2.3.3).

2.3.1 Shape of the liquid-vapor spinodal

In our early work we have measured the cavitation pressure in liquid helium using an acoustic method which will be described in Sec. 3.1. We made the first measurements on helium 3 and verified previous ones on helium 4 [C20, C21]. We mention one of the results here because of its analogy with water. We found that the cavitation line $P_{\rm cav}(T)$ in helium 3 had a smaller temperature variation than predicted by a DFT prediction. We attributed this to the existence of a minimum in the liquid-gas spinodal of helium 3, which was not present in the EoS used in the DFT treatment [C22]. Helium 3, like water, exhibits a line of density maxima; therefore, as explained by Speedy [30] (Sec. 2.2.1), if the LDM intersects the spinodal line $P_{\rm s}(T)$, the latter must have a minimum at the intersection. To check this possibility, we extrapolated sound velocity measurements to find $P_{\rm s}(T)$, and obtained a minimum of $-0.29\,$MPa around $0.4\,$K, which falls exactly on the linear extrapolation of the LDM. The negative isobaric expansion coefficient $\alpha_{\rm P}$ of helium 3 at low temperature is due to the variation of its effective mass m^* with density, and extrapolation of experimental values of m^* down to the spinodal suggests that $\alpha_{\rm P}$ remains negative at $0\,$K down to the spinodal, which is consistent with the above picture [C22].

The case of superfluid helium 4 has also been addressed. Helium 4 exhibits a line of density minima around $1\,$K, and a line of density maxima just above the superfluid transition, around $2\,$K. The density minimum arises because of the increasing number of collective excitations called *rotons*: their contribution to the expansion coefficient is negative, and exceeds the positive one of the phonons when the temperature increases. Using the simple model of Landau for superfluidity, we have estimated their relative contribution near the spinodal [C23]. As the sound velocity approaches zero whereas the roton energy does not, the positive contribution of the phonons becomes dominant, up to temperatures where the Landau model ceases to be correct. This suggests that the expansion coefficient is positive along the spinodal, and that the spinodal is monotonic. We also predicted that helium 4 remains superfluid down to the spinodal at low temperature. A more elaborate approach was proposed by Maris and Edwards which confirms these results [51]. They find that the two lines of density extrema osculate the superfluid transition at negative pressure, the three lines intersecting around $-0.53\,$MPa, above the spinodal line (around $-0.7\,$MPa at the superfluid transition, and $-0.95\,$MPa at $0\,$K).

2.3.2 A liquid-solid spinodal?

Because the liquid-solid transition is first order as the liquid-gas transition, it is possible to observe helium in a metastable state, as an overpressurized liquid. We may wonder about a possible absolute limit to this metastability, which we call a liquid-solid spinodal. It is not a spinodal in the usual sense, that is a line of diverg-

ing compressibility, because the compressibility of helium decreases with increasing pressure. Another feature could cause an instability of the overpressurized liquid.The spectrum of excitations of helium shows a local minimum, called the roton. It has a non-zero energy Δ at a finite wavenumber k_0, which is close to the reciprocal lattice vector of solid hcp helium. Schneider and Enz suggested that the transition from the superfluid to the solid was associated with the softening of the roton mode, that is Δ going to zero [52]. They were talking about the liquid-solid equilibrium line, but Δ has been measured to be around 7 K near this line. However, it is known that Δ decreases with increasing pressure. Using a linear extrapolation, we proposed that it would vanish at $P_{\Delta=0} \simeq 15$ MPa. A spatial density perturbation with the same period as the solid could then form without any energy cost, leading to an instability of the liquid towards the solid. Using the Landau model for superfluidity, we found that helium would remain superfluid at low temperature up to $P_{\Delta=0}$, and proposed that the superfluid transition temperature would reach 0 K at this pressure [C23]. With the more elaborated approach used in Ref. [51], we noticed that there was also the possibility that superfluidity breaks by a Pomeranchuk instability below this pressure [C24]. We note however that later Monte-Carlo simulations [53] found that helium 4 remains superfluid with a nonzero Δ up to at least 27.5 MPa.

2.3.3 Correction to classical nucleation theory

The experimental implications of the theoretical considerations presented in the last section depend on the possibility to prepare metastable liquid helium at large overpressures. Nucleation of the solid phase might occur before any interesting features are observed. Therefore it is important to estimate the pressure threshold for crystallization. This is also useful to discuss our acoustic crystallization experiments that will be described in Sec. 3.3. The first idea is to use CNT (Sec. 2.1.1). We find that, at 1 K, crystallization requires a pressure of around 3.7 MPa above the equilibrium freezing line at $P_\mathrm{f} = 2.53$ MPa [C19]. However, one may wonder about the validity of CNT. It predicts a critical radius less than 1 nm, whereas the thickness of the liquid-solid interface is calculated to be $1 - 1.3$ nm [38]. The capillary approximation made by CNT is therefore dubious.

We first planned to use DFT to go beyond this approximation; however, the theory we used was not able to give a full description of the liquid-solid interface (Sec. 1.3.3). Therefore we resorted to a more phenomenological modification of CNT [C25]. We took the compressibility of both phases into account, and most importantly, allowed the effective interfacial energy to vary. The interfacial energy arises because atoms in the interfacial region are displaced compared to the bulk solid. The number of such atoms per unit area of the interface is of the order of a^{-2}, where a is the interatomic spacing. We take the extra energy per unit area to be of the order of $\beta(\delta x)^2/(2a^2)$, where β is an effective spring constant between atoms and δx is the displacement of the atom. Assuming that the arrangement of the interfacial layer does not change with pressure, we take $\delta x/a$ constant, and find that the interfacial energy varies like β. We then notice that the bulk modulus B is related to β: $\beta \propto Ba \propto B\rho^{-1/3}$ with ρ the density. Finally, we take an interfacial energy which depends on pressure:

$$\sigma(P) = \sigma(P_\mathrm{f}) \, \frac{B_\mathrm{L}(P) \, \rho_\mathrm{L}(P_\mathrm{f})^{1/3}}{B_\mathrm{L}(P_\mathrm{f}) \, \rho_\mathrm{L}(P)^{1/3}} \,, \tag{2.11}$$

where (P_f) indicates values taken at the freezing pressure. This gives $\sigma(P)$ increasing almost linearly with pressure. Using this value of $\sigma(P)$ with CNT (and including the

compressibility), we find that the variation is large enough to give surprising results. The critical radius is increased to above 10 nm, which makes the capillary approximation more acceptable. Moreover, the energy barrier levels around 180 K, which corresponds to an extremely low nucleation rate and renders crystallization nearly impossible! Quantum nucleation may help, but it is difficult to estimate it here [C25]. Of course, experimentally, solid helium does exist, but this is because its nucleation occurs heterogeneously on favorable impurities on the cell walls. We will see in Sec. 3.3.2 how we have performed experiments far away from any wall.

2.4 Melting and freezing of nanoclusters

To end this chapter and before coming back to helium and water in the next one, we make a short diversion in the field of nanocrystals (NCs). NCs are crystal grains whose size is in the nanometer range. Recently, nanofabrication techniques have been developed to prepare *embedded* NCs, that is nanoinclusions inside a host matrix. They are candidates for novel optoelectronic and nonvolatile memory device applications.

We are interested in the connection between capillarity and nucleation, which can be particularly well illustrated by the thermal behavior of embedded nanoclusters. Small crystals are known to melt at a different temperature than the bulk melting point T_0; it is usually lower for free-standing nanocrystals. However, the size-dependent melting temperature is often analyzed with approximate formulas, corresponding to the absolute limits of metastability of the solid cluster, instead of accounting for nucleation at an intermediate temperature. In addition, for embedded NCs, the different interactions of the matrix with the solid and the liquid phases must be taken into account. We have addressed the issue of freezing and melting of spherical inclusions (Fig. 2.4) with a thermodynamically consistent model for nucleation of the new phase [C26]. Our model is basically a variant of CNT, where the role of the matrix is included through the contact angle θ_c of the liquid-solid interface on the matrix material, which strongly affects the nucleation behavior. In addition, the matrix curvature modifies the classical result for heterogeneous nucleation on a plane surface.

We introduce the following notations: L is the latent heat *per unit volume of the solid*, ρ_i is the density of phase i, and γ_{ij} is the surface tension between phases i and j, where i and j take the values L for liquid, S for solid, and V for vapor, respectively. For simplicity, the model assumes $\rho_L = \rho_S$ and neglects elasticity. The liquid does not necessarily wet the solid completely, especially for embedded NCs. If $\gamma_{LS} + \gamma_{LM} > \gamma_{SM}$ and $\gamma_{LS} + \gamma_{SM} > \gamma_{LM}$, there is a contact angle of the liquid on the matrix:

$$\theta_c = \arccos\left(\frac{\gamma_{SM} - \gamma_{LM}}{\gamma_{LS}}\right). \tag{2.12}$$

An interesting quantity is the temperature T_0'' at which the Gibbs' free energies of a frozen and a melted NC are equal [54]:

$$\Delta T_0'' = T_0'' - T_0 = -\frac{3\,T_0}{LR}\,(\gamma_{SV} - \gamma_{LV}) = -\frac{3\,T_0}{LR}\,\gamma_{LS}\cos\theta_c\,. \tag{2.13}$$

Our interest for this topic was triggered by Xu *et al.* [55], who proposed a nucleation model for embedded NCs, to interpret their experimental finding of a large hysteresis of melting and freezing of Ge in amorphous silica. Because the hysteresis is symmetric around T_0, they deduced from Eq. 2.13 that $\theta_c = \pi/2$ and $\gamma_{LM} \simeq \gamma_{SM}$, and performed the calculation of the nucleation temperatures for this particular case. $\theta_c = \pi/2$ is a

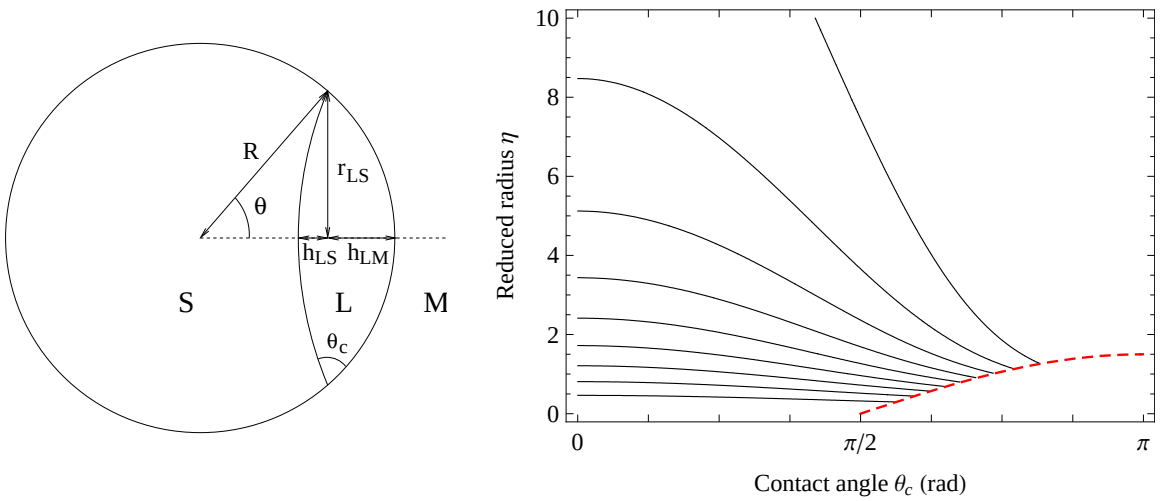

Figure 2.4: *Left*: Sketch of a liquid nucleus in the metastable solid phase. *Right*: Contour plot of the reduced energy barrier ϵ_3 for melting in the θ_c–η plane. The solid curves show the contours from $\epsilon_3 = 0.1$ (bottom) to $\epsilon_3 = 0.9$ (top), every 0.1. ϵ_3 is not defined in the lower right corner, under the dashed red line.

coincidence due to the specific properties of the system studied. It may vary for other materials. This is what motivated our generalization of the theory of Xu *et al.* to the case of an arbitrary θ_c. We have also criticized some of their numerical values and analysis [C27].

We use CNT to calculate the energy barrier for heterogeneous nucleation in a spherical inclusion of radius R at a temperature $T = T_0 + \Delta T$, with an arbitrary contact angle θ_c. We first consider melting at $T > T_0''$. The liquid phase will appear as a lenticular nuclei of volume V_L (Fig. 2.4). Let S_{LS} and S_{LM} be the areas of the interfaces between the two phases and between the liquid and the matrix, respectively; the other notations are given in Fig. 2.4. The contact angle of the liquid on the matrix being fixed at θ_c, the nuclei is fully characterized by the azimuthal angle θ of its circular boundary. We assume that the inclusion remains a sphere of radius R throughout the nucleation process. We also take the external pressure to be constant at P_0. One has then to consider the Gibbs free energy change, which writes:

$$\Delta G(\theta) = -L\,\frac{\Delta T}{T_0}\,V_L(\theta) + \gamma_{LS} S_{LS}(\theta) + (\gamma_{LM} - \gamma_{SM}) S_{LM}(\theta). \tag{2.14}$$

The detailed expressions of V_L, S_{LS} and S_{LM} are obtained with simple trigonometry and given in Ref. [C26]. For each value of the pair $(\theta_c, \Delta T)$, $\Delta G(\theta)$ exhibits a maximum which corresponds to the energy barrier for nucleation of the liquid in the solid, $E_b^{S\to L}(\theta_c, \Delta T)$. The case of freezing at $T < T_0''$ can be treated by a simple symmetry: $E_b^{L\to S}(\theta_c, \Delta T) = E_b^{S\to L}(\pi - \theta_c, -\Delta T)$. There is a correspondence between the melting of a superheated NC and the freezing of a supercooled nanodroplet. This holds only inasmuch the density difference between liquid and solid has been neglected.

Introducing non dimensional quantities, we were able to give universal plots to describe melting and freezing [C26]. We give one of them here to illustrate how the matrix curvature modifies the classical result for heterogeneous nucleation on a plane surface. We define

$$\Delta T_{max} \;=\; \frac{3\,T_0\,\gamma_{LS}}{LR}\,, \tag{2.15}$$

$$E_3 = \frac{\pi}{3}(2+\cos\theta_c)(1-\cos\theta_c)^2\,\gamma_{LS}{R_c}^2, \quad (2.16)$$

$$R_c = \frac{2\gamma_{LS}}{L}\frac{T_0}{|\Delta T|}\,. \quad (2.17)$$

ΔT_{max} is the maximum melting point shift that can be obtained for a given inclusion: $\Delta T_0'' = -\Delta T_{max}$ for $\theta_c = 0$, and $\Delta T_0'' = \Delta T_{max}$ for $\theta_c = \pi$ (see Eq. 2.13). E_3 is the energy barrier for heterogeneous nucleation on a plane surface [41]. R_c is the critical radius for homogeneous nucleation [C28]. Fig. 2.4 shows a contour plot of the reduced energy barrier $\epsilon_3 = E_b/E_3$ in the θ_c–η plane, where $\eta = R/R_c$ is a reduced radius. We have $\eta = 3\tau/2$, where $\tau = \Delta T/\Delta T_{max}$ is a reduced temperature. Fig. 2.4 shows that, for any given temperature above T_0, the classical result for heterogeneous nucleation on a plane surface is recovered for $R \gg R_c$, as expected. Note that although ϵ_3 vanishes at T_0, E_b does not: this behavior arises from the divergence of R_c and E_3 at T_0. Note also that for $\theta_c \to 0$, ϵ_3 is only defined by taking the limit, being the ratio of two vanishing quantities. One may use Fig. 2.4 to see below which size of the inclusion it becomes necessary to use the present model instead of the classical model for heterogeneous nucleation on a plane surface. The effect of confinement on melting or on freezing should be more easily seen in a system with a low or high value of θ_c, respectively. Our model also allowed us to reinterpret experimental data on the melting of indium NCs in amorphous silica [56].

Chapter 3

Experimental study of metastable liquids

There are numerous ways of preparing a liquid in a metastable state. One of the most successful ones uses emulsified samples, where the liquid to be studied is dispersed as small droplets in a host liquid that remains stable in the temperature range explored. For water, this technique is able to achieve the highest degrees of supercooling and superheating: at 0.1 MPa, liquid water was observed down to -38°C [57] and up to 300°C (see for instance [58]). The success of the method lies in the reduction of the risk of heterogeneous nucleation: small samples are less likely to contain an impurity, and as they are numerous, the ones that do will nucleate, leaving the others reach the homogeneous nucleation limit. The container is also replaced by a host liquid, which provides a clean and smooth surface, which does not affect nucleation if it wets completely the metastable liquid.

However, this technique is not useful to generate negative pressures. We have rather resorted to an acoustic technique. As an acoustic wave is a pressure oscillation, at large enough amplitudes it can stretch a liquid. In order to study a small sample far away from any wall we chose a focused, high frequency wave. We first detail the case of water. Sec. 3.1 introduces the method and the way it was used to estimate the cavitation pressure. It allows to reach higher metastability than other techniques. In Sec. 3.2, we report the density measurement that we have performed on metastable water, and the scenario we propose to explain the two cavitation limits observed in water. Finally, we go back to helium in Sec. 3.3: the positive swing of the sound wave can be used to overpressurize superfluid helium until it crystallizes; we describe the different regimes of nucleation (homogeneous and heterogeneous) that we have found.

3.1 Acoustic cavitation in water

To stretch water, we use the negative swing of a focused acoustic wave at 1 MHz. Actually, this method was introduced by Joel Nissen [59] and we used it to study cavitation in helium during our PhD [C21]. We adapeted the method to water during the PhD of Eric Herbert. A detailed account can be found in Ref. [C29]. We briefly describe the setup in Sec. 3.1.1. We can repeat a stretching experiment under given conditions a large number of times, in order to measure accurately the statistics of the cavitation events (Sec. 3.1.2). We have used two methods to estimate the threshold pressure for cavitation (Sec. 3.1.3): typically, we find around -25 MPa at room temperature. This is among the largest metastability reported for stretched water, only exceeded by one experiment based on a different technique (Sec. 3.1.4).

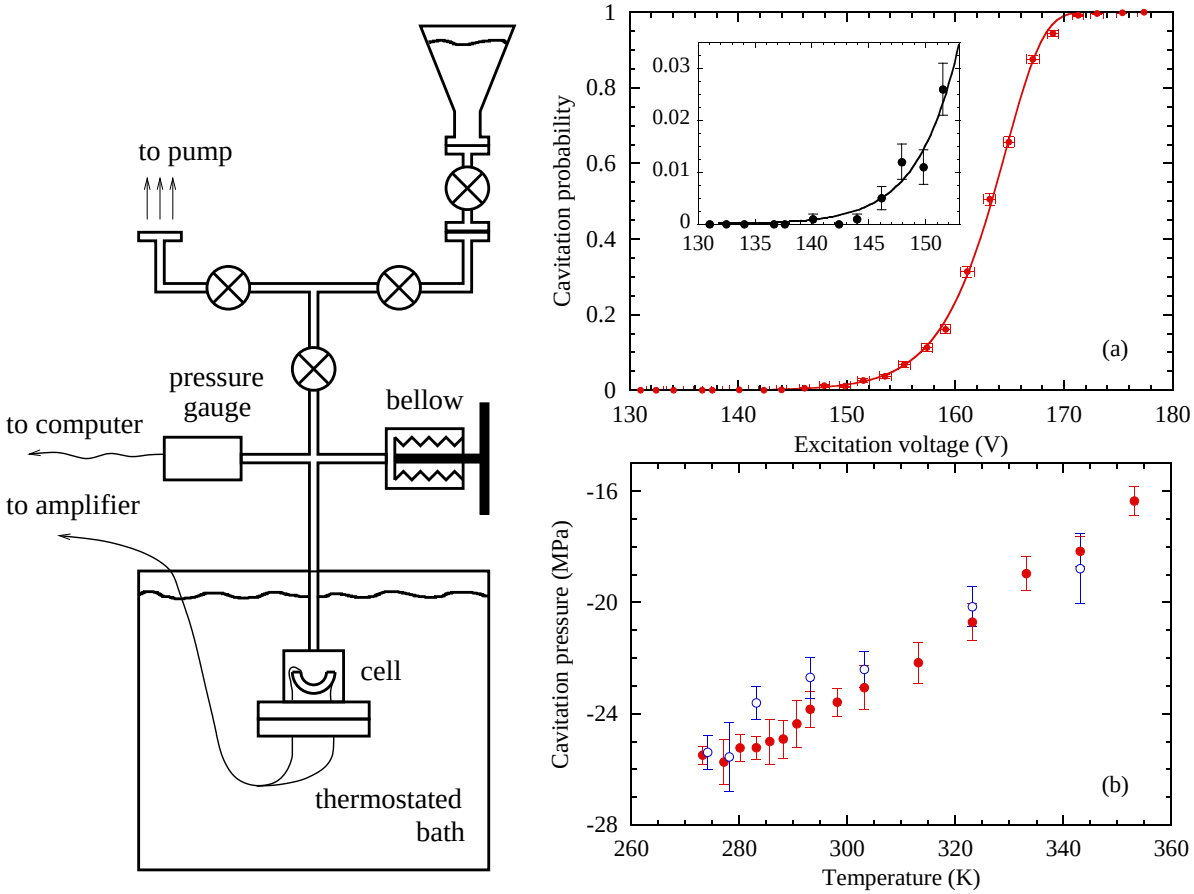

Figure 3.1: *Left panel*: Sketch of the experimental setup. The high pressure part contains the cell with the transducer, the pressure gauge and the bellow for pressure control; it can be isolated from the rest by a valve. The use of two other valves allows evacuation (with an oil pump through a nitrogen trap or a dry scroll pump) and filling from a flask with degassed water. The cell is immersed in a thermostatic bath (operated between -10 and 80°C). All the seals are made of stainless steel or bulk Teflon, except the one at the bottom of the cell, which is made with an indium wire. *Right panel*: (a) Cavitation probability versus excitation voltage for 4-cycles bursts at $T = 20$°C and $P_{\rm stat} = 1.7$ MPa. Each of the 25 data points was measured over 1000 repeated bursts. The standard deviation on the probability (calculated with the binomial law) is shown as error bars. The data are well fitted with Eq. 3.1 (solid line). The inset focuses on the low probability region, to show that zero probability is actually reached in the broad foot of the S-curve. (b) Cavitation pressure as a function of temperature. $P_{\rm cav}$ was obtained with the static pressure method (Sec. 3.1.3). Run 0 (filled circles) [C29] is compared to our preliminary results [C30] (empty circles).

3.1.1 Experimental setup

The central element of our setup (Fig. 3.1) is the ultrasonic emitter: a lead-zirconium-titanate hemispherical transducer (i.d. 16 mm, o.d. 20 mm), excited by short electrical bursts at the resonance frequency of its thickness mode (1 MHz). The hemispherical shape allows a tight focusing, far away from any walls. Acoustic maps show that only $(100\,\mu\text{m})^3$ of liquid experience a large negative pressure during around 100 ns. This brings about the conditions to observe homogeneous nucleation: a cavitation event corresponds to a nucleation rate of $10^{19}\,\text{m}^{-3}\,\text{s}^{-1}$.

Experiments can be performed in an open container. To ensure the cleanest conditions, we have also constructed a cell entirely made of stainless steel, with stainless

steel, teflon and indium seals, where the liquid can be transferred under vacuum. This allows to work with degassed water without exposing it to air. Thanks to a bellow, the cell could be operated at pressures up to 10 MPa for calibration purposes (Sec. 3.1.3).

When the excitation of the transducer is sufficient large, bubbles nucleate at the focus. They can be detected by three methods: by optical imaging, sound detection, and the echo method. The last method is based on the fact that, when a bubble appears at the center of the hemisphere, it reflects the sound wave back to the transducer surface. The corresponding random change in the transducer voltage, occurring after the time of flight of the sound wave over twice the transducer radius, is easily distinguished from the reproducible ringing down of the transducer voltage. After checking the consistency of all three methods, we have routinely used the echo.

3.1.2 Statistics of cavitation

We can set the conditions of the experiment: temperature, static pressure, excitation voltage $V_{\rm rms}$ of the transducer, burst characteristics (number of cycles, central frequency, repetition rate). When we repeat the bursts many times, we find that, for fixed conditions in some range of $V_{\rm rms}$, cavitation occurs randomly; we define the cavitation probability Σ as the ratio between the number of bursts showing a cavitation event and the total number of bursts. When scanning $V_{\rm rms}$, we find that Σ varies from 0 to 1, and exhibits a characteristic shape which we call an S-curve (Fig. 3.1 (a)). A cavitation voltage $V_{\rm cav}$ can be sharply defined as the value of $V_{\rm rms}$ at which $\Sigma = 1/2$. Moreover, we can make high-quality fits of the S-curves with the following formula:

$$\Sigma = 1 - \exp\left\{-\ln 2 \, \exp\left[\xi\left(\frac{V_{\rm rms}}{V_{\rm cav}} - 1\right)\right]\right\}, \tag{3.1}$$

where ξ and $V_{\rm cav}$ are free parameters. This is deduced for a thermally activated process through a linear expansion of the energy barrier $E_{\rm b}$ for nucleation around $V_{\rm cav}$ [C29]. ξ measures the steepness of the probability curve, and is related to the energy barrier through:

$$\xi = -\frac{V_{\rm cav}}{k_{\rm B}T}\left(\frac{\partial E_{\rm b}}{\partial V}\right)_{\Sigma=1/2}. \tag{3.2}$$

We would like to emphasize that the S-curves are very reproducible, not only for a given sample under given conditions, but also from one sample to another or for different static pressures, once the excitation voltage is renormalized by the relevant $V_{\rm cav}$. We will see more directly in Sec. 3.1.3 that the cavitation pressure is reproducible. We have only noted a difference on the low voltage side when we use tap water: its numerous impurities induce heterogeneous cavitation at lower sound amplitude, but their probability of presence at the focus is small enough to leave the main slope of the S-curve unaffected.

3.1.3 Estimate of the cavitation pressure

In the closed cell, we can work with a constant mass of water and change its volume with a bellow. We thus vary the static pressure $P_{\rm stat}$ of the liquid. Assuming that the cavitation pressure does not depend on the static pressure, an increase in $P_{\rm stat}$ requires an increase in the excitation voltage of the transducer to obtain cavitation. It can be shown [C31] that if the focusing is linear, the pressure swing in the wave $\Delta P = P_{\rm stat} - P_{\rm min}$ is proportional to $\rho(P_{\rm stat})V_{\rm rms}$, where $\rho(P_{\rm stat})$ is the density of the

liquid at rest; the marginal variation of ρ with pressure and temperature was taken into account in our analysis. Therefore, the data $P_{\rm stat}$ versus $\rho(P_{\rm stat})V_{\rm cav}$ should fall on a line crossing the axis $V_{\rm cav} = 0$ at the pressure $P_{\rm cav}$. We have thus obtained $P_{\rm cav}$ by linear extrapolation of the data taken for $P_{\rm stat}$ between 1 and 10 MPa. Taking the nonlinearities into account, the intercept thus obtained should give an upper bound for $P_{\rm cav}$ [C31].

We have also used a commercial piezoelectric needle hydrophone. Its gain is calibrated with a 14% accuracy, and it can be used only at low amplitude to avoid damage. Nevertheless, it gives a value consistent with the static pressure method. Furthermore, as it should give a lower bound for $P_{\rm cav}$ [C31], it shows that the non-linearities are limited and that we have a reliable estimate.

The final results are shown on Fig. 3.1 (b). We find a monotonous temperature variation, with $P_{\rm cav}$ becoming less negative as T is increased: it varies from -26.4 MPa at 0.1°C to -16.5 MPa at 80°C. The original motivation of the work was to discriminate between two spinodals proposed for water, by looking for a minimum in $P_{\rm cav}(T)$ (Sec. 2.2.2). There is no obvious minimum, or if a minimum exists it is very shallow. Anyhow, the experimental results disagree with both theories as regards the magnitude of $P_{\rm cav}$ ($\simeq -24$ instead of -120 MPa). In the next section we compare our results to other experiments.

3.1.4 Comparison with other experiments

The discrepancy with the theoretical predictions points towards a comparison with other experiments, to assess the quality of our experimental data. For a detailed presentation of other experiments, we refer the reader to our extensive review of the subject of cavitation in water [C32]. To summarize, we note that most experiments find much less negative pressure than we do, and a few find similar values (Fig. 3.2 (a)). The interesting point is that they are based on very different techniques: centrifugation, acoustic standing waves, or metallic Berthelot tube. We also note that the sharp increase in $P_{\rm cav}$ at low temperature in the centrifuge experiment [60] is an artifact. This has implications for the survival of trees during cold weather, while their sap is still under negative pressure: our measurements suggest that it is not limited by homogeneous cavitation of water, as was verified by centrifugation of tree shoots by Hervé Cochard at Clermont Ferrand University [C33].

There is only one other method which was reported to reach more negative pressures, as large as -140 MPa (Fig. 3.2 (b)): the use of quartz inclusions in the group of Austen Angell [49]. The principle is the following. Fractured quartz crystals are autoclaved with a known amount of ultrapure water. The fissures heal and water is trapped in inclusions at a desired density, depending on the autoclaving temperature and pressure. Angell and his group then followed Berthelot's method. The inclusion is heated along the saturated vapor pressure curve, until the last vapor bubble disappears, at a temperature $T_{\rm d}$ from which the liquid density is deduced. When the sample is cooled down, the bubble does not reappear immediately, and liquid water follows a nearly isochoric path, until cavitation occurs at $T_{\rm cav}$. To deduce $P_{\rm cav}$, they have to rely on an EoS: they chose to extrapolate the so-called HGK EoS to negative pressure. The HGK EoS is a multi-parameter EoS fitted on data measured at pressures where the liquid is stable; it is qualitatively similar to Speedy EoS (Sec. 2.2.1), but quantitatively different, giving for the coordinates of the minimum in the spinodal around 60°C and -160 MPa. There are two distinct cavitation behaviors. When $T_{\rm d} > 250$°C (autoclaving temperature higher than 400°C), $T_{\rm cav}$ is the same within ± 2°C for all

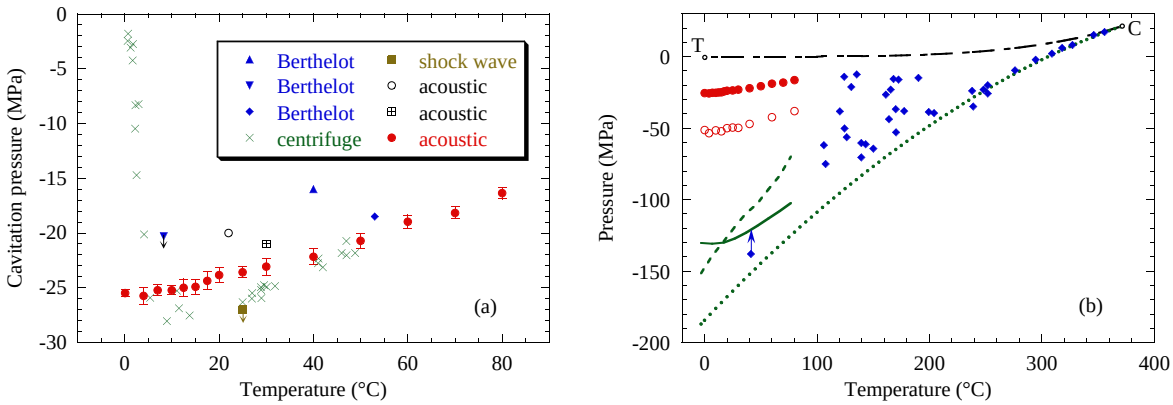

Figure 3.2: (a) Cavitation pressure versus temperature for different experiments: the corresponding method and reference are given in the legend. Only the experiments with the most negative cavitation pressures were selected, except the inclusion work, for sake of clarity. An arrow means that cavitation was not observed. The error bars on the filled circles represent the uncertainty on the pressure calibration. (b) Cavitation pressure versus temperature, calculated with CNT [C11] (dotted line), or using DFT with Speedy's EoS [30] (solid line) or with the EoS from a recent molecular dynamics simulation [61] (short-dashed line). The parameters used are $V = (10\,\mu\text{m})^3$, $\tau = 1\,\text{s}$, and Γ_0 from Eq. 2.6. The dash-dotted line shows the saturated vapor pressure from the triple point (T) to the critical point (C). Some experimental results are also shown. Filled diamonds correspond to experiments on mineral inclusions [49]; the arrow shows a correction to the pressure estimate to account for the quartz compressibility. Filled circles show our data obtained with an acoustic method, and empty circles the spinodal we once proposed to interpret them [C29].

inclusions in a given sample, whereas when $T_\text{d} < 250^\text{o}\text{C}$ (high density inclusions), T_cav is scattered. Angell and his group attribute the scatter to heterogeneous nucleation, and its source to "possibly surfactant molecules cluster destroyed by annealing at the higher temperatures".

For low density inclusions in quartz, P_cav is positive, and compares well with the maximum temperature at which liquid water can be superheated, as measured by Skripov [58]. The maximum tension of $-140\,\text{MPa}$ is obtained in one sample with high density inclusions ($0.91\,\text{g}\,\text{mL}^{-1}$ and $T_\text{d} = 160^\text{o}\text{C}$); Angell and his group report that "some [inclusions] could be cooled to -40°C without cavitation, and one was observed in repeated runs to nucleate randomly in the range 40 to 47°C and occasionally not at all" [49]: they estimate nucleation occurred at $P_\text{cav} \simeq -140\,\text{MPa}$. The fact that "no inclusion that survived cooling to 40°C ever nucleated bubbles during cooling to lower temperatures" was interpreted as an evidence that the isochore crosses the metastable LDM, thus retracing to less negative pressure at low temperature. This gives support to Speedy's scenario, at least in the sense that the LDM keeps a negative slope, deep in the negative pressure region in the $P - T$ plane.

How then can we understand the discrepancy between the quartz inclusions results and all other experiments? One may argue that other experiments observe heterogeneous nucleation. However, the reproducibility of our measurements, their lack of scattering, and their agreement with other methods, make this hypothesis unlikely. If nucleation was heterogeneous, the relevant impurities would have to be incredibly calibrated and ubiquitous to always lead to the same results.

One possibility would then be that the extrapolated EoS used in the inclusion work is wrong: thermodynamic properties of water should then exhibit dramatic changes in the negative pressure region to make all data compatible. This could happen for ex-

ample if the spinodal pressure P_s was much less negative than expected from Speedy's extrapolations or molecular dynamics simulations (Sec. 2.2.1). We have tried to make this speculation more quantitative [C29]. If cavitation in our experiments is homogeneous, then we have access to two quantities related to the EoS: the energy barrier and its slope at P_{cav}. Indeed, we write:

$$E_b(P_{cav}) = k_B T \ln\left(\frac{\Gamma_0 V \tau}{\ln 2}\right) \simeq 47.5\, k_B T, \tag{3.3}$$

taking for Γ_0 the value from Eqs. 2.6 (with $R_c = 1\,\text{nm}$) and for $V\tau$ the value for our acoustic setup. The slope is given by:

$$\left(\frac{\partial E_b}{\partial P}\right)_{P_{cav}} = -\frac{\xi k_B T}{P_{cav}}, \tag{3.4}$$

which ranges from 500 to 780 K MPa^{-1} from 0.1 to 80°C. By definition, $E_b(P_s) = 0$. To locate P_s, we extrapolate linearly E_b to zero with this slope; the result is shown on Fig. 3.2 (b). To get an idea of the accuracy of such an extrapolation, we can look at the curve $E_b(P)$ calculated with DFT [C11]: it is convex, and nearly linear in the relevant range of E_b. We would thus expect the actual P_s to be slightly more negative than the extrapolated value.

However, we have now shown unequivocally that the discrepancy between the cavitation thresholds for the acoustic method and for the inclusions is real. We will present the corresponding experiments in the next section, along with the new scenario we propose to interpret the available data.

3.2 Thermodynamic properties of metastable water

The comparison between experiments is sometimes made complicated because of the use of an extrapolated EoS to convert the measured quantities. In particular, the inclusion work has access to the density rather than the pressure. To allow a direct comparison, we have performed a measurement of the density oscillation at the acoustic focus of our experiment (Sec. 3.2.1). This shows a real discrepancy between the inclusion work and the other techniques. To explain this discrepancy, we propose that cavitation in water depends on the thermodynamic path followed in the experiment, a feature that could arise from the existence of a liquid-liquid transition at negative pressure (Sec. 3.2.2). We are currently looking for an experimental confirmation of this conjecture by measuring the sound velocity in metastable water (Sec. 3.2.3).

3.2.1 Density

To measure the density of water during the application of an acoustic burst, we have constructed, as part of the post-doc of Kristina Davitt and the PhD of Arnaud Arvengas, a fiber optic probe hydrophone (FOPH) [62]. A sketch of the setup is displayed in Fig. 3.3 (a). Reflection at the bare fiber tip immersed in the liquid is detected by a photodiode (PD) located on the other branch of a 2x2 step index coupler. The detected light power, $I(t)$, is proportional to the sum of the reflection from the bare tip,

$$R(t) = \left(\frac{n(t) - n_f}{n(t) + n_f}\right)^2, \tag{3.5}$$

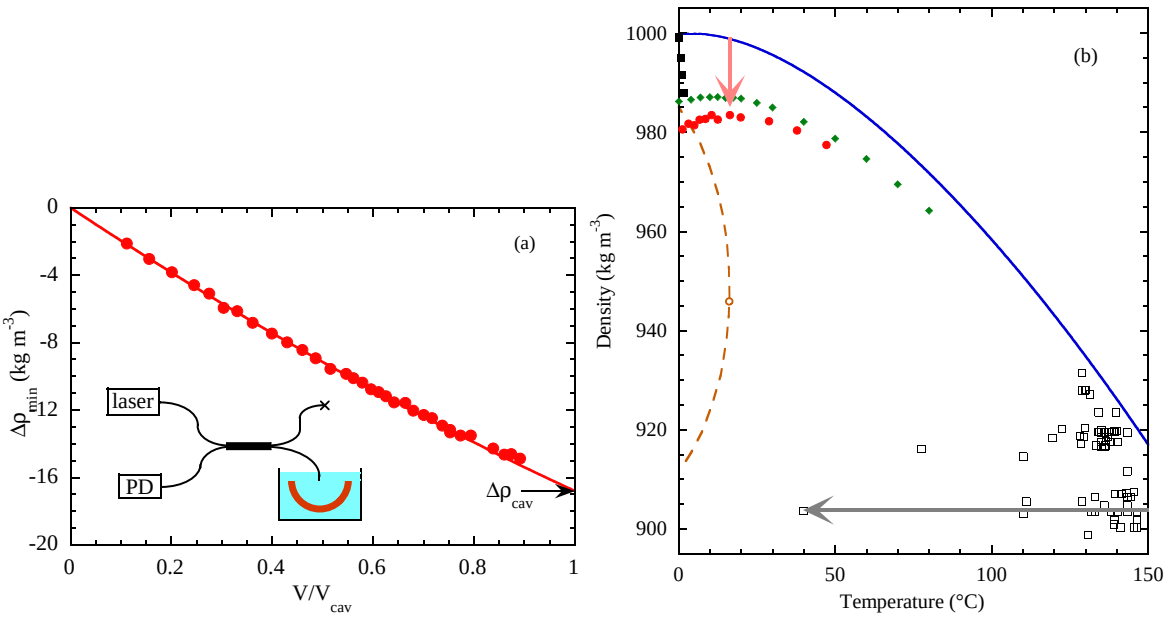

Figure 3.3: (a) Largest reduction in density with respect to the static one as a function of $V/V_{\rm cav}$ at 20°C. The solid line is a parabolic fit to the data where $V/V_{\rm cav} \leq 0.6$; data at higher fractions of $V_{\rm cav}$ illustrate that the extrapolation holds. The inset shows a sketch of the apparatus. (b) Cavitation density as a function of temperature. The red circles are averages over at least 2 experiments at each temperature. The statistical error bar, derived from the spread in 27 measurements at 20°C, is of the size of the symbols. The blue curve gives the density of water at atmospheric pressure. The green diamonds correspond to our previous estimate of $P_{\rm cav}$ with the same acoustic technique [C29], converted into density. The open black squares show the inclusions results below 150°C [64]. Also shown are results of cavitation in inclusions along the metastable ice-liquid equilibrium (closed black squares) [64]. The arrows illustrate the different thermodynamic path followed: isentropic (quasi-isothermal [C29]) in the acoustic experiment, isochoric in the usual inclusion experiments. For illustration, we show the liquid-liquid transition (brown dashed line) and its metastable critical point (MCP) (brown open circle) at negative pressure in ST2 water [65].

and a stray light term, S, included to account for any reflection from the unused arm and the non-zero cross talk of the coupler itself: $I\,(t) = I_0\,[R\,(t) + S]$. Here $n(t)$ is the index of water at the fiber tip, modulated in time by the acoustic wave, and $n_{\rm f} = 1.453$ is the index of the pure silica fiber core at the laser wavelength of 808 nm. In absence of the acoustic wave, $n(t) = n_0$ and $R(t) = R_0$. At 20°C and atmospheric pressure, $n_0 = 1.328 \pm 0.001$ at 808 nm [63], and $R_0 = 0.202\%$. With the application of an acoustic wave the detected light can be broken down into its AC and DC components, $I(t) = I_{\rm AC}(t) + I_{\rm DC}$, and their ratio computed as

$$\frac{I_{\rm AC}(t)}{I_{\rm DC}} = \frac{R\,(t) - R_0}{R_0 + S}\,. \tag{3.6}$$

From Eqs. (3.5) and (3.6) and with knowledge of S, the time varying index of water in the acoustic wave is determined. Note that the precise value of I_0 is not needed. A series of calibrated microscope immersion liquids was used to map the reflected light as a function of index. A fit with a fixed value of $n_{\rm f} = 1.453$ yielded $S = (3 \pm 0.8) \times 10^{-5}$.

To convert indices to densities, we use a semi-empirical formulation from the IAPWS [63] based on a modified Lorentz-Lorenz relation. The modulation of the reflected light intensity is very low ($\approx 10\mu$W at $0.5\,V_{\rm cav}$), therefore we use an average

over 100 bursts at each voltage to improve the signal-to-noise. At each temperature, the excitation voltage on the transducer is ramped from 0.1 to $0.6\,V_{\rm cav}$. An S-curve is measured before and after each ramp. The drift in $V_{\rm cav}$ is always less than 5%, and the average is used in the analysis.

The largest reduction in density at the focus with respect to the static density, $\Delta\rho_{\rm min}$, is plotted as a function of $V/V_{\rm cav}$ (Fig. 3.3 (a)). We note that the variation is less than linear (see below). We have extrapolated the data below $0.6\,V_{\rm cav}$ with a parabola up to $V_{\rm cav}$. We have checked at 1, 12, 20 (Fig. 3.3 (a)), and 47°C that this extrapolation reproduces correctly the data up to $0.9\,V_{\rm cav}$. For other temperatures, the ramp was limited to below $0.6\,V_{\rm cav}$ to avoid cavitation on the fiber tip. Repeated checks of the data at 20°C were performed to ensure that no damage occurred, otherwise the fiber was re-cleaved.

The cavitation densities, $\rho_{\rm cav}$, determined from extrapolations of the parabolic fit are shown in Fig. 3.3 (b). First, we compare these results with previous work in which an indirect estimate of $P_{\rm cav}$ was made by two independent methods that gave consistent values [C29] (Sec. 3.1.3). To convert between pressures and densities, we use a parabolic extrapolation of the EoS measured at positive pressure, as suggested by Speedy [30] and following the procedure of Ref. [C11]. The result is shown in Fig. 3.3 (b): the direct measurements are systematically slightly lower than the ones converted from $P_{\rm cav}$. This is consistent with the existence of non-linearities in the focusing of the sound wave, as observed in Fig. 3.3 (a). The present measurements account for the non-linearities, in contrast to the previous method [C29].

3.2.2 Path dependent cavitation

We have argued in Sec. 3.1.4 that the discrepancy between our experiment and the inclusion work is not likely to be due to impurities. We propose another, more fundamental, explanation: the nucleation mechanism depends on the thermodynamic path followed. Whereas in other experiments water is stretched starting from a stable state at room temperature, the inclusion samples enter the metastable region at high temperatures, and they are already under large tensions when they approach room temperature (Fig. 3.3 (b)). Different experiments could thus reach regions of the phase diagram where the cavitation mechanism is different. In addition, this picture is able to explain the surprising behavior of ice-melting in inclusions [64], which has hitherto been overlooked. Water in the inclusions could be frozen by cooling to −60°C. When the ice melts upon heating, because of the higher density of the liquid, the system is put under tension, until cavitation occurs. The pressure can be estimated from the metastable liquid-solid equilibrium line, which extrapolates linearly from the stable part, as confirmed experimentally down to −24 MPa [66]. Surprisingly, the largest $P_{\rm cav}$ obtained with this method is −22.8 MPa (Fig. 3.3 (b), lowest closed black square): cavitation occurred at 1.7°C during melting, in an inclusion which cavitated at −103.7 MPa with the usual isochoric liquid cooling method [64]. This internal discrepancy in the inclusion work is strikingly similar to the one between the inclusion work and other techniques.

Nucleation occurs by thermal density fluctuations when their energy ($\approx k_{\rm B}T$) is able to overcome the energy barrier, $E_{\rm b}$, due to surface tension which separates the metastable liquid from the stable vapor phase. In classical nucleation theory (CNT), using the surface tension of bulk water, $\sigma = 72\,{\rm mN\,m^{-1}}$, to compute $E_{\rm b}$, one finds $P_{\rm cav} \simeq -180\,{\rm MPa}$ at room temperature [C29]. This is not so far from the inclusion estimate. However, nucleation could occur through an intermediate metastable state

which would lower E_b: this is called the Ostwald step rule, often invoked in crystallization, and recently verified experimentally [67]. For cavitation, as P_{cav} scales as $\sigma^{3/2}$ in CNT, to explain -30 MPa at 20°C requires an effective $\sigma = 22\,\mathrm{mN\,m^{-1}}$ [C29]. Furthermore, simulations of a model globular protein have shown how the vicinity of a fluid-fluid MCP in the phase diagram of the protein largely reduces E_b for its crystallization [68]. The same result was obtained with DFT [69]. In the case of water, we propose that E_b at a given temperature is not a monotonic function of pressure. This could be caused by an MCP at negative pressure, separating two liquid polymorphs, which has been found in some simulations [65,70] (an example is shown in Fig. 3.3 (b)). This is in addition to the MCP found by all molecular dynamics simulations at positive pressure in the supercooled regions [44, 48, 70–72]. In experiments that stretch water from room temperature, nucleation would thus be affected by the vicinity of the MCP at negative pressure. On the other hand, the isochoric path followed by the inclusions goes through a region of large tension at high temperature. Thus, it may avoid the critical region and yield P_{cav} expected from CNT with σ of bulk water. Far from the MCP, any path should lead to the same P_{cav}. Indeed, this is the situation above 300°C, where the inclusion method agrees with direct superheating experiments [49].

To confirm this scenario, we will: (i) study acoustic cavitation at higher temperature, and (ii) measure the EoS of the metastable liquid to look for a signature of an MCP, for example, via evidence of an anomaly in the compressibility. To motivate further simulations, we estimate the deficit number of molecules in the critical nucleus : using our cavitation statistics [C29] and invoking the nucleation theorem [73], we find 270 at 40°C for the acoustic experiment, versus $\simeq 120$ expected from CNT for the inclusion results.

3.2.3 Sound velocity

We briefly describe our current efforts to measure the sound velocity in metastable water. During her post-doc, Kristina Davitt has developed a time-resolved Brillouin scattering experiment. When light is scattered from a liquid, its frequency can remain the same (elastic scattering), or it can be shifted by absorption or emission of a phonon (Brillouin scattering). The frequency shift is proportional to the product of the refractive index of the liquid and the speed of sound. The aim of the experiment is to measure this shift, but only during the short time (100 ns) where the liquid is at maximum negative pressure. The refractive index being known from the FOPH data (Sec. 3.2.1), the sound velocity is deduced. The combination of the Brillouin and FOPH experiments will give the equation of state of metastable water down to the acoustic cavitation threshold. The Brillouin experiment is particularly difficult, because many repetitions of the acoustic bursts are needed to accumulate enough scattered photons: each measurement thus takes several hours, which requires a high stability of the system. Preliminary results are shown in Fig. 3.4

3.3 Acoustic crystallization in helium

We now get back to helium, in which the acoustic setup used for cavitation can also be used to study crystallization. As can be seen from its phase diagram (see Fig. 1 in the Introduction), a positive pressure swing can bring the liquid above its freezing line (at 2.53 MPa). This opens the way to investigate how the superfluid transition evolves when the liquid density is increased (Sec. 2.3.2). But the first step is to know

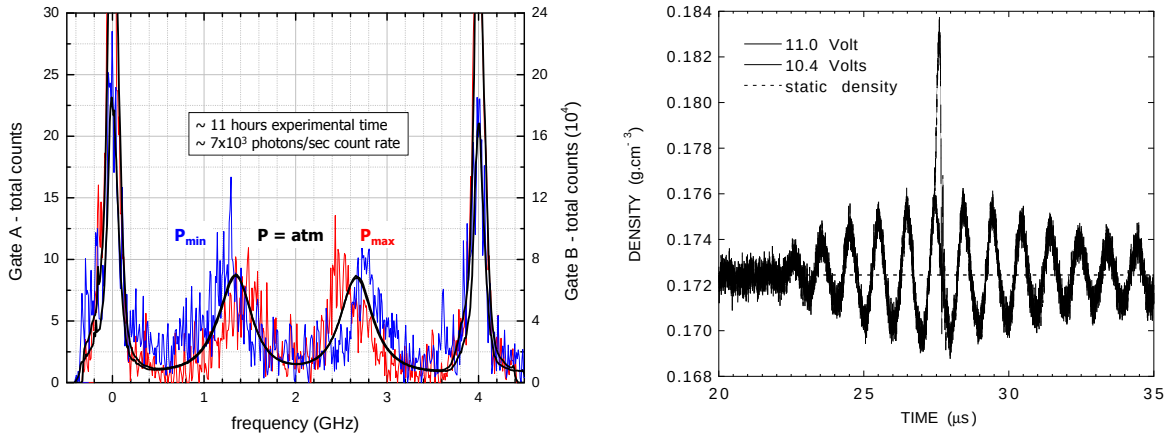

Figure 3.4: *Left*: Experimental spectra of the light scattered from water: the black smooth line shows a spectrum at atmospheric pressure, with the Rayleigh peaks on the sides and the Brillouin peaks at the center. The red and blue curves correspond to spectra from the focus of the acoustic wave at the minimum and maximum pressure, respectively; they are noisier than the black line because of the comparatively smaller number of photons, but they allow to measure the change in sound velocity. *Right*: Two recordings of the helium density at the acoustic focus as a function of time. One trace corresponds to an excitation (10.4 V) below the crystallization threshold; the other one (11.0 V) is superimposed on the first one and shows a peak corresponding to the nucleation of solid helium.

how far the liquid can be overpressurized, and this is what we have studied in a series of experiments.

3.3.1 Heterogeneous crystallization

A first observation of acoustic crystallization was made by Xavier Chavanne during his post-doc [C34]. The aim of the experiment was at first to obtain a direct measurement of the liquid density. An approach based on the same principle as the fiber optic hydrophone (Sec. 3.2.1) was used. A glass plate was introduced at the acoustic focus, and a laser beam focused at the glass-helium interface. The focused laser spot is around $30\,\mu$m, much less than the acoustic wavelength of $360\,\mu$m. Because of the difference in refractive indices, the light is reflected. When a sound wave is present, the reflection is modulated because of the density variations in helium. Averaging repeated measurements and following a reasoning similar to the one presented in Sec. 3.2.1, the time trace of the density oscillation is obtained (see Fig. 3.4). It was found that high density peaks appeared at a well defined threshold, with a probability increasing from 0 to 1 in a narrow range of transducer voltage (similarly to cavitation, see Sec. 3.1.2). At large excitation, the density saturated at $191\,\mathrm{kg\,m^{-3}}$, indicative of hcp solid helium. Near the threshold, the maximum density reached gives the size of the crystallite, around $15\,\mu$m in diameter for the trace on Fig. 3.4.

The growth rate of the nucleated crystals is very high, around $100\,\mathrm{m\,s^{-1}}$, close to the speed of sound, $366.3\,\mathrm{m\,s^{-1}}$. This is possible because of the ability of helium crystals to grow very fast at low temperature [2], in contrast to classical crystals where for instance the evacuation of latent heat introduces a resistance to growth. The nucleation density can be compared to theory. For this, it is easier to convert it into pressure, using a short extrapolation of the experimental equation of state of the stable liquid: we obtained $3.0 \pm 0.03\,$MPa, 0.47 MPa above the freezing line. This is 2 to 3 orders of

magnitude larger than in previous experiments (cited in Ref. [C34]), but much lower than the 7 MPa overpressure predicted by classical nucleation theory (Sec. 2.1.1). At low temperature, as the prediction of CNT diverges, one expects quantum nucleation through the energy barrier to take the relay; even in that case, the overpressure needed for crystallization should saturate around 4.1 MPa [74]. This shows that nucleation on the glass plate is heterogeneous, but on impurities less favorable to solid than in previous experiments, where graphite particles may play a role [75]. We should also mention that heterogeneous cavitation and non-linear focusing were studied in the same setup. Different kinds of heterogeneous nucleation regimes were found, depending on the position on the glass plate: the nucleation pressure were estimated to be -0.3 MPa, and even 0 MPa on a weak spot slightly out of focus [C35]. This is much less negative than the previous estimate for cavitation without the glass plate (between -1.04 and -0.8 MPa) [C20], and quite surprising, as liquid helium wets perfectly most surfaces, so that the glass plate was not expected to affect nucleation. For high amplitude sound wave, the measured density oscillation becomes distorted, with sharp and narrow positive peaks, and broad and shallow negative swings. These features, due to the curvature of the equation of state (the compressibility varies with pressure) are quantitatively reproduced in simulations of the focusing [C31]. A consequence is that the static pressure method described in Sec. 3.1.3 gives an upper bound on the actual cavitation pressure.

3.3.2 Homogeneous crystallization

After observing heterogeneous crystallization of helium on a glass plate, we tried to observe homogeneous nucleation in the bulk liquid.

Hemispherical geometry

The first attempt simply used the same system as for heterogeneous crystallization (Sec. 3.3.1), but with the glass plate removed [C36]. The lens was kept in order to improve the sensitivity of the detection at high pressure, for which the acoustic focus is in the focal plane of the lens. It is better to start with a high static pressure to achieve crystallization, in order to reach higher sound amplitudes before cavitation occurs during the negative swing of the wave, destroying the focusing of the wave. Looking at the light scattered from the focus, we were able to detect nucleation events between 1.8 and 2.53 MPa. The variation of the nucleation voltage with pressure was linear, and extrapolated to -0.945 MPa. We therefore concluded that we were observing cavitation, near the spinodal pressure predicted at -0.965 MPa. This means that an excitation voltage of 105 V produced a pressure swing of $2.5 - (-0.94) = 3.44$ MPa. By switching the polarity of the excitation voltage, we tried to reach a higher positive pressure, before cavitation occurred during the next negative swing. We did not see any nucleation up to 265 V, which in a linear approximation corresponds to a maximum pressure of $2.5 + 265/1053.44 = 11$ MPa. To achieve higher pressures, we directly discharged high voltage from a capacitor into the transducer. We observed cavitation at 340 V, reversed the polarity, and did not observe nucleation up to 1370 V. The above reasoning lead us to conclude that no crystallization occurred up to 16.3 MPa at 55 mK. This seems to exceed the prediction from classical nucleation theory. This lead us to propose a modified version which suggested that homogeneous crystallization could be nearly impossible, because the variation of surface energy with pressure would prevent the energy barrier to become sufficiently low (Sec. 2.3.3).

Spherical geometry

We then turned to spherical geometry, obtained by putting two hemispherical transducers together. Our hope was to increase the non-linearities of the focusing, thus reaching larger peak positive pressures while keeping negative swings small enough to avoid cavitation. As the focal length of the lens in helium changes with pressure, the signal is eventually lost. We decided to remove this lens and to focus the laser beam from a lens outside. We now used the low frequency (132 kHz) breathing mode of the transducer, to leave more time for the crystals to grow. At the beginning of his post-doc, Ryosuke Ishiguro performed a careful study of the time of flight of the signals [C37]. Cavitation events were observed when starting from low static pressure, and crystallization events when starting from high static pressure, at a time shifted by half a period from the cavitation events. We thus reached the limit of homogeneous nucleation. The problem is that we do not know the nucleation pressure, and the non-linearities render the estimate difficult. This also leads us to reconsider the previous search for crystallization in the experiments with hemispherical geometry and a 1 MHz wave (Sec. 3.3.2). The time of flight could not be studied as accurately as in the spherical geometry, where echoes of the sound wave across the diameter of the sphere served to determine the sphere radius accurately. Our main argument to conclude that the nucleation events we observed at that time were due to cavitation, was the positive slope of the static pressure as a function of nucleation voltage. It might be that the non-linearities of the sound wave resulted in this behavior, even if crystallization actually occured.

Conclusion and prospects

Overview

At first sight, water, the familiar everyday liquid, and helium, the paradigm of a quantum fluid, seem to live in unrelated worlds. Yet in our opinion, they provide a connex playground to illustrate and investigate the basic concepts of capillarity, wetting, phase transitions and metastability. Because of its purity, helium allows experiments to reach the conditions to test theoretical predictions which are otherwise sometimes obscured by extrinsic factors. Its theoretical description has also reached a very high degree of elaborateness, and at the same time some puzzles remain, like supersolidity. Water is full of surprises, and each model developed to reproduce some its fascinating properties may lack some other feature, which calls for extensive experimental studies.

More specifically, we have seen that the wetting properties of the grain boundaries between helium crystals (Sec. 1.1) allowed to test ideas coming from the field of metallurgy. If cavitation in helium seems fairly well understood, crystallization in the metastable liquid (Sec. 3.3) still keeps some puzzles. The current efforts are focused on supersolidity; in our group, Sébastien Balibar is exploring the relation between crystal quality and elastic anomalies.

Our study of cavitation in water (Sec. 3.1) ends with a huge interrogation mark. We have found a new *no man's land* in the phase diagram: in addition to the one that exists in the supercooled range (between homogeneous crystallization of the liquid and crystallization of amorphous ice), one lies at negative pressure where cavitation depends on the thermodynamic path followed. It is a strong encouragement to investigate further the stretched liquid state, whose properties have up to now only been grazed.

Prospects

An immediate follow-up of our work is to extend the measurements of the acoustic cavitation density to high temperatures, in order to see if it merges with the cavitation density obtained in the inclusion work. We cannot use the fiber optic probe hydrophone at high temperature, because its positionning requires an open container. However, the static pressure method can be used even at temperature above 100°C in the high pressure cell. We have seen that it gives an overestimate of the actual threshold, but the difference gets smaller with higher temperature.

Although the acoustic technique we have been using is very well suited to produce reproducible, large negative pressures, thermodynamic measurements on the stretched liquid state are delicate because of the short timescale of the experiment (100 ns per burst). Recently, the group of Abraham Stroock at Cornell University was able to produce large *static* pressures down to -24 MPa [76]. They use liquid filled cavities ($100\,\mu$m in diameter) in a hydrogel (*artificial tree*, see Fig. 3.5); the structure of the

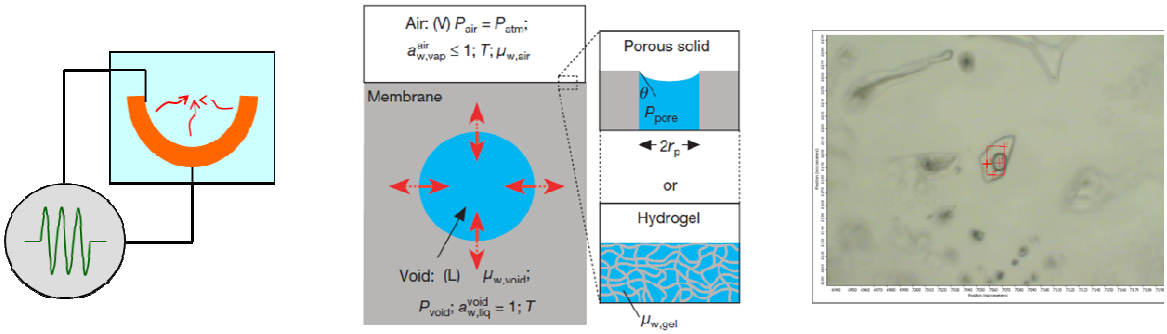

focused ultrasound artificial tree inclusion in quartz

Figure 3.5: Three setups that we will use to measure properties of liquid water at negative pressure.

gel allows to equilibrate the liquid with its undersaturated vapor outside. When the system reaches a uniform chemical potential, set by a saturated salt solution outside the gel, the liquid in the cavity is put under tension. We are starting a collaboration with Abraham Stroock to combine his technique with optical measurements of the liquid properties. Control of the vapor pressure will allow a fine tuning of the chemical potential. We plan to use Brillouin scattering (but this time in a much easier static experiment) to get the sound velocity in the stretched liquid, and hence the equation of state. This will however provide data at moderate metastability. Therefore, we want also to use quartz inclusions prepared by a group at Orléans University during the SURCHAUF project (P.I.: Lionel Mercury) (Fig. 3.5); they can reach pressures in the range of $-100\,\mathrm{MPa}$ [77]. Brillouin scattering was already performed on such samples [78], but we would like to repeat these study in a more systematic way. The combination of density and sound velocity as a function of temperature would allow to check equations of state in the metastable range. As some inclusions can be supercooled without cavitation, we even hope to explore the doubly metastable region, where the liquid is metastable with respect to the vapor and to the solid. We can also think of performing other types of measurements, e.g. Raman scattering. With this battery of tests, we will try to detect a signature of a possible metastable critical point at negative pressure.

F. Caupin's publications cited in the text

[C1] Sasaki, S., Caupin, F., and Balibar, S. (2007) Wetting properties of grain boundaries in solid He-4. *Physical Review Letters*, **99**, 205302.

[C2] Sasaki, S., Caupin, F., and Balibar, S. (2008) Optical observations of disorder in solid helium 4. *Journal of Low Temperature Physics*, **153**, 43–76.

[C3] Caupin, F., Sasaki, S., and Balibar, S. (2008) Supersolidity and disorder in solid helium 4. *Journal of Low Temperature Physics*, **150**, 267–275.

[C4] Caupin, F., Sasaki, S., and Balibar, S. (2008) Absence of grain boundary melting in solid helium. *Journal of Physics-Condensed Matter*, **20**, 494228.

[C5] Balibar, S. and Caupin, F. (2008) Supersolidity and disorder. *Journal of Physics-Condensed Matter*, **20**, 173201.

[C6] Sasaki, S., Ishiguro, R., Caupin, F., Maris, H., and Balibar, S. (2006) Superfluidity of grain boundaries and supersolid behavior. *Science*, **313**, 1098–1100.

[C7] Sasaki, S., Ishiguro, R., Caupin, F., Maris, H., and Balibar, S. (2007) Supersolidity and superfluidity of grain boundaries. *Journal of Low Temperature Physics*, **148**, 665–670.

[C8] Balibar, S. and Caupin, F. (2008) Comment on "Observation of unusual mass transport in solid hcp He-4". *Physical Review Letters*, **101**, 189601.

[C9] Caupin, F. (2007) Comment on "Capillary filling of anodized alumina nanopore arrays". *Physical Review Letters*, **98**, 259601.

[C10] Caupin, F., Herbert, E., Balibar, S., and Cole, M. (2008) Comment on "Nanoscale water capillary bridges under deeply negative pressure" [Chem. Phys. Lett. 451 (2008) 88]. *Chemical Physics Letters*, **463**, 283–285.

[C11] Caupin, F. (2005) Liquid-vapor interface, cavitation, and the phase diagram of water. *Physical Review E*, **71**, 051605.

[C12] Caupin, F., Cole, M., Balibar, S., and Treiner, J. (2008) Absolute limit for the capillary rise of a fluid. *Europhysics Letters*, **82**, 56004.

[C13] Caupin, F. and Minoguchi, T. (2004) Density functional theory of freezing of superfluid helium 4. *Journal of Low Temperature Physics*, **134**, 181–186.

[C14] Caupin, F. and Minoguchi, T. (2005) Density functional theory of the interface between solid and superfluid helium 4. *Journal of Low Temperature Physics*, **138**, 331–336.

[C15] Ancilotto, F., Barranco, M., Caupin, F., Mayol, R., and Pi, M. (2005) Freezing of He-4 and its liquid-solid interface from density functional theory. *Physical Review B*, **72**, 214522.

[C16] Caupin, F., Ancilotto, F., Barranco, M., Mayol, R., and Pi, M. (2007) Freezing of helium-4: Comparison of different density functional approaches. *Journal of Low Temperature Physics*, **148**, 731–736.

[C17] Balibar, S. and Caupin, F. (2002) The limits of metastability of liquid helium. Imre, A. R., Maris, H. J., and Williams, P. R. (eds.), *Liquids under negative pressure*, vol. 84 of *NATO Science Series II: Mathematics, Physics and Chemistry*, pp. 145–160, Springer.

[C18] Balibar, S. and Caupin, F. (2003) Metastable liquids. *Journal of Physics-Condensed Matter*, **15**, S75–S82.

[C19] Caupin, F., Balibar, S., and Maris, H. (2003) Limits of metastability of liquid helium. *Physica B-Condensed Matter*, **329**, 356–359.

[C20] Caupin, F. and Balibar, S. (2001) Cavitation pressure in liquid helium. *Physical Review B*, **64**, 064507.

[C21] Caupin, F. (2001) *Cavitation dans l'hélium 3 : un liquide de Fermi à pression négative*.

[C22] Caupin, F., Balibar, S., and Maris, H. (2001) Anomaly in the stability limit of liquid He-3. *Physical Review Letters*, **87**, 145302.

[C23] Caupin, F. and Balibar, S. (2002) Quantum statistics of metastable liquid helium. Imre, A. R., Maris, H. J., and Williams, P. R. (eds.), *Liquids under negative pressure*, vol. 84 of *NATO Science Series II: Mathematics, Physics and Chemistry*, pp. 201–214, Springer.

[C24] Caupin, F., Edwards, D., and Maris, H. (2003) Thermodynamics of metastable superfluid helium. *Physica B-Condensed Matter*, **329**, 185–186.

[C25] Maris, H. and Caupin, F. (2003) Nucleation of solid helium from liquid under high pressure. *Journal of Low Temperature Physics*, **131**, 145–154.

[C26] Caupin, F. (2008) Melting and freezing of embedded nanoclusters. *Physical Review B*, **77**, 184108.

[C27] Caupin, F. (2007) Comment on "Large melting-point hysteresis of Ge nanocrystals embedded in SiO2". *Physical Review Letters*, **99**, 079601.

[C28] Balibar, S. and Caupin, F. (2006) Nucleation of crystals from their liquid phase. *Comptes Rendus Physique*, **7**, 988–999.

[C29] Herbert, E., Balibar, S., and Caupin, F. (2006) Cavitation pressure in water. *Physical Review E*, **74**, 041603.

[C30] Herbert, E. and Caupin, F. (2005) The limit of metastability of water under tension: theories and experiments. *Journal of Physics-Condensed Matter*, **17**, S3597–S3602.

[C31] Appert, C., Tenaud, C., Chavanne, X., Balibar, S., Caupin, F., and d'Humières, D. (2003) Nonlinear effects and shock formation in the focusing of a spherical acoustic wave - Numerical simulations and experiments in liquid helium. *European Physical Journal B*, **35**, 531–549.

[C32] Caupin, F. and Herbert, E. (2006) Cavitation in water: a review. *Comptes Rendus Physique*, **7**, 1000–1017.

[C33] Cochard, H., Barigah, T., Herbert, E., and Caupin, F. (2007) Cavitation in plants at low temperature: is sap transport limited by the tensile strength of water as expected from Briggs' Z-tube experiment? *New Phytologist*, **173**, 571–575.

[C34] Chavanne, X., Balibar, S., and Caupin, F. (2001) Acoustic crystallization and heterogeneous nucleation. *Physical Review Letters*, **86**, 5506–5509.

[C35] Chavanne, X., Balibar, S., and Caupin, F. (2002) Heterogeneous cavitation in liquid helium 4 near a glass plate. *Journal of Low Temperature Physics*, **126**, 615–620.

[C36] Werner, F., Beaume, G., Hobeika, A., Nascimbene, S., Herrmann, C., Caupin, F., and Balibar, S. (2004) Liquid helium up to 160 bar. *Journal of Low Temperature Physics*, **136**, 93–116.

[C37] Ishiguro, R., Caupin, F., and Balibar, S. (2006) Homogeneous nucleation of crystals by acoustic waves. *Europhysics Letters*, **75**, 91–97.

References

[1] de Gennes, P. G., Brochard-Wyard, F., and Quéré, D. (2003) *Capillarity and Wetting Phenomena: Drops, Bubbles, Pearls, Waves*. Springer-Verlag.

[2] Balibar, S., Alles, H., and Parshin, A. Y. (2005) The surface of helium crystals. *Reviews of Modern Physics*, **77**, 317–370.

[3] Dash, J. G. and Wettlaufer, J. S. (2006) The physics of premelted ice and its geophysical consequences. *Reviews of Modern Physics*, **78**, 695–741.

[4] Pollet, L., Boninsegni, M., Kuklov, A. B., Prokof'ev, N. V., Svistunov, B. V., and Troyer, M. (2007) Superfluidity of grain boundaries in solid He-4. *Physical Review Letters*, **98**, 135301.

[5] Lipowsky, R. (1986) Melting at grain-boundaries and surfaces. *Physical Review Letters*, **57**, 2876–2876.

[6] Alsayed, A. M., Islam, M. F., Zhang, J., Collings, P. J., and Yodh, A. G. (2005) Premelting at defects within bulk colloidal crystals. *Science*, **309**, 1207–1210.

[7] Franck, J. P., Kornelsen, K. E., and Manuel, J. R. (1983) Wetting of fcc He4 grain boundaries by fluid He4. *Physical Review Letters*, **50**, 1463–1465.

[8] Kim, E. and Chan, M. H. W. (2004) Probable observation of a supersolid helium phase. *Nature*, **427**, 225–227.

[9] Kim, E. and Chan, M. H. W. (2004) Observation of superflow in solid helium. *Science*, **305**, 1941–1944.

[10] Telschow, K., Rudnick, I., and Wang, T. G. (1974) Observation of the critical velocity peak in superfluid films. *Physical Review Letters*, **32**, 1292–1295.

[11] Wilks, J. (1967) *The properties of liquid and solid helium*. Clarendon Press.

[12] Ray, M. W. and Hallock, R. B. (2008) Observation of unusual mass transport in solid hcp He-4. *Physical Review Letters*, **100**, 235301.

[13] Ray, M. W. and Hallock, R. B. (2008) Reply to comment on "Observation of unusual mass transport in solid hcp He-4". *Physical Review Letters*, **101**, 189602.

[14] Cohan, L. H. (1938) Sorption hysteresis and the vapor pressure of concave surfaces. *Journal of the American Chemical Society*, **60**, 433–435.

[15] Cole, M. W. and Saam, W. F. (1974) Excitation spectrum and thermodynamic properties of liquid films in cylindrical pores. *Physical Review Letters*, **32**, 985–988.

[16] Saam, W. F. and Cole, M. W. (1975) Excitations and thermodynamics for liquid-helium films. *Physical Review B*, **11**, 1086–1105.

[17] Alvine, K. J., Shpyrko, O. G., Pershan, P. S., Shin, K., and Russell, T. P. (2006) Capillary filling of anodized alumina nanopore arrays. *Physical Review Letters*, **97**, 175503.

[18] Morishige, K. and Shikimi, M. (1998) Adsorption hysteresis and pore critical temperature in a single cylindrical pore. *The Journal of Chemical Physics*, **108**, 7821–7824.

[19] Butt, H., Cappella, B., and Kappl, M. (2005) Force measurements with the atomic force microscope: technique, interpretation and applications. *Surface Science Reports*, **59**, 1–152.

[20] Yang, S. H., Nosonovsky, M., Zhang, H., and Chung, K. (2008) Nanoscale water capillary bridges under deeply negative pressure. *Chemical Physics Letters*, **451**, 88–92.

[21] Liu, L., Chen, S., Faraone, A., Yen, C., and Mou, C. (2005) Pressure dependence of fragile-to-strong transition and a possible second critical point in supercooled confined water. *Physical Review Letters*, **95**, 117802.

[22] Mallamace, F., Broccio, M., Corsaro, C., Faraone, A., Wanderlingh, U., Liu, L., Mou, C., and Chen, S. H. (2006) The fragile-to-strong dynamic crossover transition in confined water: nuclear magnetic resonance results. *The Journal of Chemical Physics*, **124**, 161102.

[23] Liu, D., Zhang, Y., Chen, C., Mou, C., Poole, P. H., and Chen, S. (2007) Observation of the density minimum in deeply supercooled confined water. *Proceedings of the National Academy of Sciences*, **104**, 9570–9574.

[24] Mallamace, F., Broccio, M., Corsaro, C., Faraone, A., Majolino, D., Venuti, V., Liu, L., Mou, C., and Chen, S. (2007) Evidence of the existence of the low-density liquid phase in supercooled, confined water. *Proceedings of the National Academy of Sciences*, **104**, 424–428.

[25] Mallamace, F., Branca, C., Broccio, M., Corsaro, C., Mou, C., and Chen, S. (2007) The anomalous behavior of the density of water in the range 30 K $<$ T $<$ 373 K. *Proceedings of the National Academy of Sciences*, **104**, 18387–18391.

[26] Mallamace, F., Corsaro, C., Broccio, M., Branca, C., González-Segredo, N., Spooren, J., Chen, S., and Stanley, H. E. (2008) NMR evidence of a sharp change in a measure of local order in deeply supercooled confined water. *Proceedings of the National Academy of Sciences*, **105**, 12725–12729.

[27] Kim, H., Gatica, S. M., and Cole, M. W. (2007) Interaction thresholds for adsorption of quantum gases on surfaces and within pores of various shapes. *The Journal of Physical Chemistry A*, **111**, 12439–12446.

[28] Cahn, J. W. and Hilliard, J. E. (1958) Free energy of a nonuniform system. I. Interfacial free energy. *The Journal of Chemical Physics*, **28**, 258–267.

[29] The International Association for the Properties of Water and Steam (1994), Release on the surface tension of ordinary water substance, september 1994.

[30] Speedy, R. J. (1982) Stability-limit conjecture. an interpretation of the properties of water. *The Journal of Physical Chemistry*, **86**, 982–991.

[31] Ramakrishnan, T. V. and Yussouff, M. (1979) First-principles order-parameter

theory of freezing. *Physical Review B*, **19**, 2775–2794.

[32] Haymet, A. D. J. and Oxtoby, D. W. (1981) A molecular theory for the solid–liquid interface. *The Journal of Chemical Physics*, **74**, 2559–2565.

[33] Dalfovo, F., Dupont-Roc, J., Dupont-Roc, N., Stringari, S., and Treiner, J. (1991) Freezing of liquid helium at zero temperature: a density functional approach. *Europhysics Letters*, **16**, 205–210.

[34] Moroni, S. and Senatore, G. (1991) Theory of freezing for quantum fluids: crystallization of 4He at zero temperature. *Europhysics Letters*, **16**, 373–378.

[35] Denton, A. R., Nielaba, P., Runge, K. J., and Ashcroft, N. W. (1990) Freezing of a quantum hard-sphere liquid at zero temperature: a density-functional approach. *Physical Review Letters*, **64**, 1529–1532.

[36] Dalfovo, F., Lastri, A., Pricaupenko, L., Stringari, S., and Treiner, J. (1995) Structural and dynamical properties of superfluid helium: a density-functional approach. *Physical Review B*, **52**, 1193–1209.

[37] Oxtoby, D. W. (1991) Crystallization of liquids: a density functional approach. Hansen, J., Levesque, D., and Zinn-Justin, J. (eds.), *Liquids, Freezing and Glass Transition*, pp. 145–191, no. Session L1, 1989 in Les Houches, Elsevier Science Publishers.

[38] Pederiva, F., Ferrante, A., Fantoni, S., and Reatto, L. (1994) Quantum theory of solid-liquid coexistence and interface in He4. *Physical Review Letters*, **72**, 2589–2592.

[39] Debenedetti, P. G. (1996) *Metastable liquids*. Princeton University Press.

[40] Fisher, J. C. (1948) The fracture of liquids. *Journal of Applied Physics*, **19**, 1062–1067.

[41] Volmer, M. (1929) Über keimbildung und keimwirkung als spezialfälle der heterogenen katalyse. *Zeitschrift für Elektrochemie*, **35**, 555–561.

[42] Chen, C., Fine, R. A., and Millero, F. J. (1977) The equation of state of pure water determined from sound speeds. *The Journal of Chemical Physics*, **66**, 2142–2144.

[43] Speedy, R. J. and Angell, C. A. (1976) Isothermal compressibility of supercooled water and evidence for a thermodynamic singularity at -45°C. *The Journal of Chemical Physics*, **65**, 851–858.

[44] Debenedetti, P. G. (2003) Supercooled and glassy water. *Journal of Physics: Condensed Matter*, **15**, R1669–R1726.

[45] Speedy, R. J. (2004) Comment on "Supercooled and glassy water". *Journal of Physics: Condensed Matter*, **16**, 6811–6813.

[46] Debenedetti, P. G. (2004) Reply to comment on "Supercooled and glassy water". *Journal of Physics: Condensed Matter*, **16**, 6815–6817.

[47] Poole, P. H., Sciortino, F., Essmann, U., and Stanley, H. E. (1992) Phase behaviour of metastable water. *Nature*, **360**, 324–328.

[48] Angell, C. A. (2008) Insights into phases of liquid water from study of its unusual Glass-Forming properties. *Science*, **319**, 582–587.

[49] Zheng, Q., Durben, D. J., Wolf, G. H., and Angell, C. A. (1991) Liquids at large negative pressures: water at the homogeneous nucleation limit. *Science*, **254**, 829–832.

[50] Cahn, J. W. and Hilliard, J. E. (1959) Free energy of a nonuniform system. III. Nucleation in a two-component incompressible fluid. *The Journal of Chemical Physics*, **31**, 688–699.

[51] Maris, H. and Edwards, D. (2002) Thermodynamic properties of superfluid He-4 at negative pressure. *Journal of Low Temperature Physics*, **129**, 1–24.

[52] Schneider, T. and Enz, C. P. (1971) Theory of the Superfluid-Solid transition of he4. *Physical Review Letters*, **27**, 1186–1188.

[53] Vranješ, L., Boronat, J., Casulleras, J., and Cazorla, C. (2005) Quantum Monte Carlo simulation of overpressurized liquid he-4. *Physical Review Letters*, **95**, 145302.

[54] Reiss, H., Mirabel, P., and Whetten, R. L. (1988) Capillarity theory for the "coexistence" of liquid and solid clusters. *The Journal of Physical Chemistry*, **92**, 7241–7246.

[55] Xu, Q., et al. (2006) Large Melting-Point hysteresis of Ge nanocrystals embedded in SiO2. *Physical Review Letters*, **97**, 155701.

[56] Tagliente, M. A., Mattei, G., Tapfer, L., Antisari, M. V., and Mazzoldi, P. (2004) Thermal behavior of indium nanoclusters in ion-implanted silica. *Physical Review B*, **70**, 075418.

[57] Taborek, P. (1985) Nucleation in emulsified supercooled water. *Physical Review B*, **32**, 5902–5906.

[58] Skripov, V. P. and Pavlov, P. A. (1970) Explosive boiling of liquids and fluctuation nucleus formation. *High Temperature*, **8**, 782–787.

[59] Nissen, J. A., Bodegom, E., Brodie, L. C., and Semura, J. S. (1989) Tensile strength of liquid He4. *Physical Review B*, **40**, 6617–6624.

[60] Briggs, L. J. (1950) Limiting negative pressure of water. *Journal of Applied Physics*, **21**, 721–722.

[61] Yamada, M., Mossa, S., Stanley, H. E., and Sciortino, F. (2002) Interplay between time-temperature transformation and the liquid-liquid phase transition in water. *Physical Review Letters*, **88**, 195701.

[62] Staudenraus, J. and Eisenmenger, W. (1993) Fiberoptic probe hydrophone for ultrasonic and shock-wave measurements in water. *Ultrasonics*, **31**, 267–273.

[63] The International Association for the Properties of Water and Steam (1997), Release on the refractive index of ordinary water substance as a function of wavelength, temperature and pressure.

[64] Zheng, Q. (1991) *PhD thesis*.

[65] Brovchenko, I., Geiger, A., and Oleinikova, A. (2005) Liquid-liquid phase transitions in supercooled water studied by computer simulations of various water models. *The Journal of Chemical Physics*, **123**, 044515.

[66] Henderson, S. J. and Speedy, R. J. (1987) Melting temperature of ice at positive

and negative pressures. *The Journal of Physical Chemistry*, **91**, 3069–3072.

[67] Chung, S., Kim, Y., Kim, J., and Kim, Y. (2009) Multiphase transformation and Ostwald's rule of stages during crystallization of a metal phosphate. *Nature Physics*, **5**, 68–73.

[68] ten Wolde, P. R. and Frenkel, D. (1999) Homogeneous nucleation and the Ostwald step rule. *Physical Chemistry Chemical Physics*, **1**, 2191–2196.

[69] Talanquer, V. and Oxtoby, D. W. (1998) Crystal nucleation in the presence of a metastable critical point. *The Journal of Chemical Physics*, **109**, 223–227.

[70] Brovchenko, I. and Oleinikova, A. (2008) Multiple phases of liquid water. *ChemPhysChem*, **9**, 2660–2675.

[71] Debenedetti, P. G. and Stanley, H. E. (2003) Supercooled and glassy water. *Physics Today*, **56**, 40–46.

[72] Stanley, H., Kumar, P., Franzese, G., Xu, L., Yan, Z., Mazza, M., Buldyrev, S., Chen, S., and Mallamace, F. (2008) Liquid polyamorphism: possible relation to the anomalous behaviour of water. *The European Physical Journal Special Topics*, **161**, 1–17.

[73] Oxtoby, D. W. and Kashchiev, D. (1994) A general relation between the nucleation work and the size of the nucleus in multicomponent nucleation. *The Journal of Chemical Physics*, **100**, 7665–7671.

[74] Uwaha, M. (1983) Quantum nucleation of solids. *Journal of Low Temperature Physics*, **52**, 15–30.

[75] Balibar, S., Mizusaki, T., and Sasaki, Y. (2000) Comments on heterogeneous nucleation in helium. *Journal of Low Temperature Physics*, **120**, 293–314.

[76] Wheeler, T. D. and Stroock, A. D. (2008) The transpiration of water at negative pressures in a synthetic tree. *Nature*, **455**, 208–212.

[77] Shmulovich, K. I., Mercury, L., Thiéry, R., Ramboz, C., and Mekki, M. E. (2009) Experimental superheating of water and aqueous solutions. *Geochimica et Cosmochimica Acta*, **73**, 2457–2470.

[78] Alvarenga, A. D., Grimsditch, M., and Bodnar, R. J. (1993) Elastic properties of water under negative pressures. *The Journal of Chemical Physics*, **98**, 8392–8396.

De l'hélium à l'eau : capillarité et métastabilité dans deux liquides d'exception

Frédéric CAUPIN

Dans ce manuscrit, nous illustrons les concepts de capillarité et de métastabilité avec des exemples mettant en jeu surtout l'hélium ou l'eau. L'étude de liquides métastables peut apporter des informations originales sur leur structure. Dans le cas de l'eau, nous avons mesuré à quel degré le liquide pouvait être porté au-delà de l'équilibre avec la vapeur : nous avons ainsi exploré la région des pressions négatives, où le liquide est mis sous tension mécanique, à densité réduite. Nos résultats indiquent une nouvelle anomalie de l'eau dans cette région. Dans l'hélium, nous avons exploré une autre sorte de métastabilité, cette fois en appliquant une pression supérieure à la pression de cristallisation : le liquide devient plus dense et métastable comparé au solide. Cela soulève des questions intéressantes à propos du maintien de la superfluidité.

Tout d'abord, nous nous intéressons à la capillarité, en portant une attention particulière à l'interface liquide-solide de l'hélium et à l'interface liquide-vapeur de l'eau. Nous présentons également quelques éléments concernant l'adsorption dans des pores. Ensuite nous discutons la métastabilité d'un point de vue théorique ; nous donnons une relation quantitative avec la capillarité et faisons le lien entre la cavitation et certaines anomalies de l'hélium et de l'eau. Nous traitons aussi des propriétés quantiques de l'hélium métastable et faisons une brève digression à propos de la nucléation en géométrie confinée. Enfin, nous récapitulons nos expériences sur la cavitation dans l'eau et la cristallisation dans l'hélium, basées sur la même technique acoustique.

From helium to water: capillarity and metastability in two exceptional liquids

Frédéric CAUPIN

In this manuscript, we illustrate the concepts of capillarity and metastability with examples mostly involving helium or water. The study of metastable liquids can bring original information about their structure. In the case of water, we have measured how far the liquid could be brought away from equilibrium with the vapor: we have thus explored the region of negative pressures, where the liquid is put under mechanical tension at reduced density. Our results point out a new anomaly of water in this region. In helium, we have explored another kind of metastability, this time by applying pressure above freezing: the liquid becomes denser and metastable compared to the solid. This raises interesting questions about the persistence of superfluidity.

First, we focus on capillarity, with a particular attention given to the liquid-solid interface of helium and the liquid-vapor interface of water. Some elements concerning adsorption in pores are also given. Then we discuss metastability from a theoretical point of view; we give a quantitative relation with capillarity, and make the connection between cavitation and some anomalies of helium and water. We also adress the quantum properties of metastable helium, and make a brief digression about nucleation in confined geometry. Finally, we summarize our experiments on cavitation in water and crystallization in helium, based on the same acoustic technique.